A comparative analysis of the precipitation extremes obtained from TRMM satellite and rain gauges datasets over a semi-arid region

by Mahbod, M., Shirvani, A. and Veronesi F.

DOI: https://doi.org/10.1002/joc.5824

Full title: **A comparative analysis of the precipitation extremes obtained from TRMM satellite and rain gauges datasets over a semi-arid region**

Short title (running head)**: Precipitation extremes by TRMM & rain gauges**

Mehdi Mahbod[1], Amin Shirvani[2], Fabio Veronesi[3]

1. Department of Water Sciences & Engineering, College of Agriculture, Jahrom University, Jahrom, I.R. Iran. Postal Code: 74137-66171. Email: mehdi.mahbod@jahrom.ac.ir; mahbod001@yahoo.com .
2. Department of Water Engineering, Oceanic and Atmospheric Research Center, College of Agriculture, Shiraz University, Shiraz Postal Code: 71441-33111, Iran. E-mail: am_shirvani@hotmail.com ; ashirvani@shirazu.ac.ir .
3. Crop and Environment Sciences Department, Harper Adams University. Newport, Shropshire, TF10 8NB – United Kingdom

Corresponding author: Mehdi Mahbod

A comparative analysis of the precipitation extremes obtained from TRMM satellite and rain gauges datasets over a semi-arid region

Abstract

The objectives of this research were to compare precipitation extremes obtained from TRMM satellite and those of rain gauges over a semi-arid area in Iran. Extreme precipitation indices (EPIs) (i.e. the number of days with precipitation value over 10 mm, maximum duration of wet and dry days, the number of days with precipitation over the 95th percentile, total precipitation higher than the 95th percentile, and maximum daily precipitation) were calculated across Fars province, Iran, 2000–2014 at seasonal time scales. The gauges data were interpolated at the spatial resolution of 0.25^{o} × 0.25^{o} to match the 3B42 data using Inverse Distance Weighting (IDW). Then EPIs from the two datasets were compared with each other. The findings showed that mean values computed from gauges and satellite data did not present any significant differences among all of the extreme indices. Furthermore, their variances presented a good level of congruence. Finally, the majority of indices presented a satisfactory correlation between the two dataset. To evaluate the prediction of extreme events in different temporal and tolerated distances, a fuzzy method was used. The results showed that the percentage of grid cells with useful predictions tripled with extending spatial tolerance by just one pixel. To evaluate methods of eliminating the uncertainty of probable missing rainfall data and the seasonal changes in rainfall averages, probabilistic methods based on Weibull distribution and truncated geometric distribution were employed to eliminate uncertainties in estimation of extreme precipitation amounts and extreme wet periods. The results showed that as to extreme precipitation amounts, a satisfactory method could not be drawn for arid southern regions of Fars, Iran .Similarly, as to extreme wet periods, the consistency between gauges and satellite data could not be improved significantly.

Keywords: Extreme precipitation, TRMM satellite, Rain gauges, Fars province.

1. Introduction

Precipitation is an important meteorological parameter in the climatic, agricultural, and hydrological studies of a region. Traditionally, precipitation is measured in rain gauges with a good accuracy. However, precipitation is a parameter with high spatial variations. Most rain gauges are located in regions of easy reach by human operators—they have a very low density in regions far from cities or on very high mountains (Nastos *et al*., 2016). This creates a clear issue of coverage, which can be partially solved with remote sensing technologies (e.g. radar systems and earth-observing satellites), which are used to continuously estimate precipitation at global scales.

In the past two decades, some satellites-based programs including Global Precipitation Climatology Project (GPCP) (Huffman *et al*., 2001), the Climate Prediction Centre Morphing technique (CMORPH; Joyce *et al*., 2004), Tropical Rainfall Measuring Mission (TRMM), Multi-sensor Precipitation Analysis (TMPA) (Huffman *et al*. 2007), Precipitation Estimation from Remotely Sensed Information using Artificial Neural Network (PERSIANN; Hsu *et al*., 1997), PERSIANN Cloud Classification System (PERSIANN-CCS; Hong *et al*., 2007), PERSIAN-CDR (Ashouri *et al*., 2015) and Global Satellite Mapping of Precipitation

(GSMaP; Ushio *et al*., 2009) have been developed to estimate precipitation. Moazami *et al*. (2016) evaluated the daily precipitation data of four widely-used satellite rainfall estimates (TMPA-3B42V7, TMPA-3B42RT, PERSIANN, and CMORPH) on a dense rain gauge network over six regions in Iran with various physiographic and climatic conditions. They concluded that the most accurate estimation of the daily precipitation was obtained from TMPA-3B42V7. Other studies for evaluation of the data estimated by the TRMM satellite across different parts of the world include studies over Iran (Javanmard *et al*., 2010; Alijanian *et al*. 2017), Greece (Nastos *et al*., 2016), India (Prakash *et al*., 2016b, 2018), Bangladesh (Tarek *et al*., 2017), Ethiopia (Awange *et al*., 2016), China (Zhao and Yatagai., 2014; Cai *et al*., 2016; Zhao *et al*., 2017), and the United States of America (Prat and Nelson, 2014; Chen *et al*., 2013; Qiao *et al*.,2014). In all of these studies, acceptable results were obtained from the TRMM data. The TRMM ended its mission in 2015 and was replaced with Global Precipitation Measurement (GPM) (Prakash *et al*., 2016a; Skofronick-Jackson *et al*., 2017; Manz *et al*. 2017).

To examine the precipitation phenomenon in a region, the calculation and evaluation of the extreme precipitation values are crucial for management and decision-making under extreme environmental conditions, including flood and drought. Various studies have been conducted regarding extreme precipitation, including studies by Hajani and Rahman (Australia, 2018), Shrestha *et al*. (Koshi basin river, 2017), Najafi and Moazami (2016), Wang *et al*. (China and USA, 2014), Raveh-Rubin and Werneli (Mediterranean region, 2015) and Tangang *et al*. (Indonesia, 2017). However, only a few studies have been conducted for the comparison of extreme precipitation values obtained from satellite data and rain gauges. Lockhoff *et al.* (2014) evaluated European precipitation extremes obtained by GCPC and found them to be less than satisfactory. Katiraie-Boroujerdy *et al*. (2017) used PERSIAN-CDR data to evaluate the extreme precipitation indices (EPIs) over a subtropical semi-arid region. They concluded that PERSIANN-CDR mostly underestimated the indices. Pombo and Oliveira (2015) calculated the maximum annual daily precipitation in Angola based on ground rain gauges and TRMM satellite. They indicated that TRMM underestimated maximum annual daily precipitation. Nastos *et al*. (2013) compared ETCCDI extreme indices of the Mediterranean Sea obtained from ground rain gauges and TRMM satellite data and reported a significant difference between the two datasets. Bharti *et al*. (2016) used the TRMM 3B42 version 7 (3B42) precipitation data to investigate extreme rainfall events during the monsoon season over the Northwest Himalaya for the period 1998-2013. However, their study did not include a comparison between satellite and ground data. Considering the limited number of studies regarding the evaluation of extreme precipitation values of TRMM satellite especially in Iran, the researchers have compared the estimated precipitation extremes from 3B42 and rain gauges in a semi-arid region of Iran.

2. Material and methods

2.1 Study area and data used

The relative dry climate coupled with the indiscriminate withdrawal of groundwater has intensified pressure on water resources and exacerbated the water crisis in Iran. This calls for an enhanced management of water resources, which must start with a better management of meteoritic water. Fars province is one of the centres of livestock and arable farming in Iran, which is located between the latitudes $27^{\circ}3'$ and $31^{\circ}42'$ and the longitudes $50^{\circ}30'$ and $55^{\circ}36'$ (Figure 1a), partly covered by the Zagros mountain chain northwardly. It is also close to the Persian Gulf southwardly and Khuzestan Plain borders westwardly (Azadi and Karimi-Jashni, 2016). According to the digital elevation model (DEM) maps generated by Shuttle Radar Topography Mission (SRTM) a wide range of altitudes is observed in Fars with a minimum elevation of just 114 m, and a maximum of 3922 m above sea level (Figure 1b). The unique geographic location of Fars along with the high variation of altitudes result in different climatic zones, namely, temperate semi-arid, temperate desert arid, cold semi-arid, temperate Mediterranean, cold desert arid, warm desert arid, and warm semi-arid based on modified De-Marton's classification method (Soufi, 2004).

Figure 2 (a) indicates average of annual precipitation (RTOT, mm), mean number of wet days in a year (NWET, day), average of annual precipitation over all wet days (INT, mm day^{-1}), and the 95th percentile from the empirical (wet day) distribution functions (Q95, mm), obtained from the rain gauges of Far province, 2000-2014. RTOT ranges from 125 mm in the southern and eastern regions of the province to near 1000 mm in the northwestern parts. Zagros Mountain chain plays a significant role in the precipitation diversity of Fars. Although a similar spatial trend is obvious for NWD, RTOT, INT, and Q95, the spatial variation coefficient (CV) for these parameters were not the same across the rain gauges, so that CV for Q95, INT, NWD, and RTOT were 0.21, 0.24, 0.27 and 0.47, respectively. Therefore, the highest CV was related to RTOT, and when the rainfall was normalized with the number of rainy days (INT), CV decreased by 50%. Precipitation over the Middle East and Iran is usually related to moist air masses originated in the Mediterranean Sea and the southern water bodies (Arabian sea, Oman Sea, Persian Gulf, Red Sea, and north Indian ocean; Raziei *et al*. 2012). To identify rainy months, the climatological means of monthly precipitation over Fars province is presented in Figure 3 for the period 2000 -2014, which shows the rainy months are from November to April, with only 3 percent of annual precipitation occurring from May to the end of October and with the highest monthly precipitation occurring in December and January.

In order to maintain the quality of rain gauges data, of the total number of stations available (n=137), 90 stations were selected, with continuous data between January^{1st} 2000 to December29th 2014. The dataset was obtained from Fars Regional Water Organization. The coordinates and statistical characterizations (mean, minimum and maximum, and standard deviation) of the gauges under investigation for the annual time scale are provided in Table S1 as Supporting Information. According to Zolina *et al*. (2005, 2010), heavy precipitation and dry and wet periods are practically insensitive to gaps in daily time series lower than 10%. However, according to Fars Regional Water Organization, there are less than 5% missing values in the reported precipitation data. Hence, to increase certainty, the researchers used Double Mass Curve method (DMC; McCuen, 2016) to check the relative homogeneity of the precipitation data. Therefore, the researchers plotted accumulated rainfall at each station against the average accumulation for two adjacent stations with a high correlation. The r^2 values accounted for over 99% of the statistical variance. In other words, only less than one percent of the statistical variance remained unexplained. When plotted curves for DMC were checked, missing values were only found in station No. 29. To remedy the problem, the researchers adjusted the precipitation values in the suspicious days for this station as proposed by Ouma *et al*. (2012).

The TRMM satellite was launched on 9 November 1997 and it ended collecting data on April 15, 2015.The 3B42 product covers the latitude range 50^{o}S-50^{o}N with the basic temporal resolution of 3 hours. The daily precipitation data of TRMM 3B42 Version 7 (3B42) has been downloaded from the Goddard Earth Sciences Data and Information Services Centre (GES-DISC, http://mirador.gsfc.nasa.gov) with spatial resolution of 0.25×0.25 and temporal resolution of one day for the period of 1 January 2000 to 29 December 2014. The geographic location of 3B42 grid cells, which are located in the area of rain gauges data interpolation, are depicted in Figure 4. The researchers also compared the daily rainfall data between the rain gauges and the nearest 3B42 grid cells and obtained the following results: correlation coefficient= 0.67, root mean square error= 8.5 mm, prediction of detection= 0.58, false alarm ratio= 0.51, and critical success index= 0.36 (all measures are described in Moazami *et al*. (2016)).

2.2 Interpolation

As the location of the rain gauges does not match the gridded 3B42 data, it is first necessary to interpolate the rain gauge data at $0.25^{\circ} \times 0.25^{\circ}$ for each day. Four methods are commonly used to interpolate precipitation values as follows: kriging, inverse distance weighted (IDW) and thin plate spline (TPS) (Webster and Oliver, 2007), as well as a method suggested by Haylock *et al.* (2008). The latter involves a three step approach where monthly means are interpolated using TPS, then daily local precipitation are normalized (by dividing them for the monthly mean for the same location) and the interpolation of anomalies using kriging. Therefore, the researchers applied a five-fold cross-validation (James et al. 2013) framework to determine which method performed the best for this particular dataset. Results (Table 1) are computed using the mean absolute error as an index that measures the average difference between observed and estimated rainfall values. These indicate that IDW and Haylock's method are the most accurate method for the large majority of years. Moreover, their average accuracy over the entire time period is essentially the same. The researchers finally decided to use IDW, since it is the simplest method to apply; it provides accurate results; and it is easy to automate in ArcGIS.

Technically, raster layers for 5,499 days (from 1 January 2000 to 29 December 2014) were prepared, based on the daily data of the rain gauges for Fars province. The necessity to perform such a large number of daily interpolations caused us to automate the task using inverse distance weighted (Pombo and Oliviera, 2015) interpolation in Python within the ArcGIS 10.3 framework. The objective of any interpolation method is to estimate the value of a parameter at unmeasured locations based on a discrete set of observations, i.e. rain gauges. However, in locations far from gauges there may be a discrepancy between estimated data and real rainfall amount, which creates a certain amount of uncertainty in the interpolated values. Inverse distance is not capable of assessing this level of uncertainty. Other algorithms, e.g. kriging, are capable of interpolating univariate data and provide local uncertainty. Nonetheless, in this study the number of gauges is not sufficient for this method to be applied successfully (Webster and Oliver, 2007). Additionally, the assumption that rain gauges provide a realistic measurement of precipitation events has also been questioned in the literature (Wehbe *et al*., 2017). Thus, adding another layer of uncertainty check seems unjustifiable, as no interpolation method would be capable of minimizing uncertainty further.

2.3 Extreme precipitation indices

In order to assess extreme rainfall events, in terms of their magnitude and intensity, some indices have been proposed by the Expert Team on Climate Change Detection and Indices (ETCCDI) (Zhang *et al.* 2011) as indicated in Table 2. The indices R10mm and R20mm show the number of days with precipitation higher than 10 and 20 mm, respectively. As shown in Figure 2, mean intensity for all rain gauges except for one was lower than 20 mm. As a result, the researchers considered only R10mm in this paper. The two indices CWD and CDD indicate the maximum number of wet or dry durations in a period of time. The precipitation intensity (INT) is equivalent to SDII (Table 2), which is investigated in section 4.1 (climatological statistics). The percentile indices could be obtained by comparing the value of daily precipitation with a threshold value. If it is higher than the threshold on a certain day, that is considered to be a day with extreme rainfall. The threshold value is obtained from the 95 or 99th percentile of long term series of precipitation in a location. Since climate in area under investigation is semi-arid, the 99th percentiles were excluded. Likewise, since the occurrence of five consecutive rainy days was nonexistent in most grid cells even in rainy seasons, the researchers did not consider Rx5day, either.

Although some researchers have used ETCCDI indices to study extreme precipitation (e.g. Heidinger *et al.* 2018, Li *et al.* 2018), others have raised objections to these indices due to uncertainties for the estimation of maximum consecutive wet/dry days (CWD/CDD) and the sensitivity of these indices to lost data. Likewise, similar objections have been raised to percentile indices such as R95pTOT (Zolina *et al.* 2009, Zolina *et al.* 2013, Leander *et al.* 2014). For percentile indices, changes in total rainfall or the number of wet days have been reported as sources of uncertainty in the trend analysis. Thus, alternative methods have been presented to eliminate uncertainty (Zolina *et al.* 2009, Leander *et al.* 2014). The employed methods for percentile indices and wet/dry spells (CWD/CDD) are explained in sections 2.3.1 and 2.3.2, respectively.

2.3.1. Percentile extremes

There are two absolute and relative general approaches to calculate the percentile indices. In the absolute approach, the amount of rainfall events that exceeds the percentile of long-term rainfall time series would be considered as extreme precipitation value (similar to the definition of ETCCDI, Table 2). However, in the relative approach, the amount of rainfall in extreme events is divided by the total rainfall of a single year or season. This approach was adopted by Klein Tank and Können (2003) for the first time. The main feature of this approach is that it considers the effect of a change in the total rainfall on changes in the amount of extreme events. However, in some areas or seasons with few wet days, this method will produce some uncertainty (Zolina *et al.*, 2009). The increase in heavy precipitation could well be a function of variations in total precipitation or it could be due to increased precipitation and decreased number of wet days (e.g. Zolina *et al*. 2004, 2008). To counteract this uncertainty, Zolina *et al* (2009) provided Distribution of Fractional Contribution (DFC) based on gamma distribution for daily rainfall to calculate relative percentile indices in a season. They mentioned that this proposed percentile extreme index is more stable, especially when precipitation extremes are estimated from a limited number of wet days of the seasonal or monthly time series. Leander *et al.* (2014) addressed another uncertainty of proposed index by Zolina *et al*. (2009) - the fact that a change in the mean also affects the estimated percentile extreme even when the shape of the distribution is unchanged. Therefore, a trend within the percentile extreme index doesn't essentially represent a modification within the distributional form related to an amplified response of maximum precipitation.

In this study, the researchers evaluated the estimations of relative percentile precipitation extremes of 3B42 data by employing the method proposed by Leander *et al*. (2014). According to Klein Tank and Können (2003) definition, $\mathrm{R95pTOT_r}$ could be approximated as follows (Leander *et al.* 2014):

$$\mathrm{R95pTOT}_r \approx \frac{1}{\mu_w}\int_Q^\infty x g_w(x)dx \tag{1}$$

where Q is long term 95th percentile, μ_w and g_w are the average and the probability density function of wet days precipitation. Leander *et al*. (2014) proposed to use 95th percentile in a single season (q) instead of Q. Therefore, the modified $\mathrm{R95pTOT}_r$ would be as follows:

$$\mathrm{RS95pTOT} \approx \frac{1}{\mu_w}\int_q^\infty x g_w(x)dx = \int_{\frac{q}{\mu_w}}^\infty x' g_w{}'(x')dx' \tag{2}$$

where x' is $\frac{x}{\mu_w}$ and $g_w{}'$ is the density function of x'. Leander *et al*. (2014) proposed two-parameter Weibull distribution for g_w. Therefore, the probability density of shifted (as δ) Weibull distribution is given as follows:

$$g_w(x) = \frac{c}{a}\left(\frac{x-\delta}{a}\right)^{c-1} exp\left[-\left(\frac{x-\delta}{a}\right)^c\right], x \geq \delta \tag{3}$$

where a and c are scale and shape parameters, and δ is the wet-day threshold precipitation (i.e. 1 mm). The final expression for $RS95pTOT$ would be as Equation (4).

$$RS95pTOT \approx \frac{a\Gamma\left(1+\frac{1}{c}\right)}{\delta + a\Gamma\left(1+\frac{1}{c}\right)}\left[\frac{0.05\delta}{a\Gamma\left(1+\frac{1}{c}\right)} + 1 - P\left(\frac{1}{c}+1, -log(0.05)\right)\right] \quad (4)$$

where Γ is gamma function and P is the normalized incomplete gamma function. For estimation of c, two-parameter Weibull distribution was fitted to the wet-days amounts (over δ) using maximum likelihood method (Wilks, 2011).

In addition, results were obtained on an individual basis per season to account for the ever-changing precipitation patterns and weather regimes, which affected the accuracy of the satellite-based estimates as well as the uncertainty of the in situ measurements. The seasons were outlined as winter: December to February (DJF), spring: March to May (MAM), summer: June to August (JJA), and autumn: September to November (SON). According to Leander et al. (2014) seasons with 10 or more wet days were considered for calculating $RS95pTOT$. Due to low rate of precipitation in summer, this season was excluded from this study. Since the highest amount and frequency of rainfall occur in winters and the limit to provide all of results, the researchers presented them for winters in details, while for the other seasons (spring and autumn) the overall results were reported

2.3.2. Wet/dry spells

To distinguish between dry and wet days, 1 mm precipitation was taken as the threshold value as proposed by Groisman and Knight (2008). Furthermore, wet periods (WPs) and dry periods (DPs) were considered separately for the wet season (October-March) and dry season (April-September). Traditional seasonal schedules would lead to noticeable uncertainties when estimating the durations of WPs and DPs because wet and dry periods are not necessarily confined within seasonal boundaries. (Zolina *et al.*, 2013). Consequently, the researchers attributed WPs to the season in which they began. However DPs were attributed to the season that included longer durations of the dry periods. This was considered necessary because of long dry periods in the dry season. Maximum values of WPs and DPs (CWD and CDD, respectively) were considered by ETCCDI as an extreme precipitation parameter in a season or year (Table 2).

The analysis of wet and dry periods is highly sensitive to the continuity of records. In order to remove this limitation from the current study, as suggested by Zolina *et al*. (2013), the researchers fitted Truncated Geometric Distribution (TGD) to the data. The probability density function (PDF) of the TGD is given as follows (Zolina *et al*., 2013):

$$P(x_i = k) = \frac{1}{1-(1-p)^N} p(1-p)^{k-1} \tag{5}$$

where x_i is the duration of the continuous wet (dry) period in days, p is the distribution parameter, which is the inverse of mean duration (wet/dry) in the standard geometric distribution, and N is the maximum of WPs/DPs. The PDF derivation of TGD is explained in details by Zolina *et al*. (2013). By using Equation (5), percentiles related to a given wet/dry duration could be estimated and vice versa. To examine the goodness of fitness of the TGD on the data, Chi-square test was applied, which showed that there was not any significant differences between the distribution of WPs/DPs and TGD at the grid cells at 5% significance level.

2.4 Data analysis

The Pearson correlation coefficient (r) was used to assess the correlation between 3B42 and RG results. The bias ratio (BR; the ratio of 3B42 results and RG) was used to quantitatively compare the results of the two datasets. The two-sample t-test (Snedecor and Cochran, 1989) and the Mann–Whitney U test (MW; Stedinger *et al*., 1993) were used to check the homogeneity of the means. Moreover, the Levene test- based on the median- and F test were used to check the homogeneity of the standard deviations of the two datasets (Nordstokke *et al*., 2011). All statistical tests were performed at 5% significance level.

Besides the point by point evaluation approaches, fuzzy verification or neighbourhood method (Ebert 2008) was also employed with the purpose of allowing slight temporal/spatial displacements of 3B42 estimates for extreme events. The 'maximum displacement allowed' refers to a local neighbourhood (or window) surrounding the grid cell of interest. For instance, for a given spatiotemporal scale of 5 pixels and 3 days (hereafter shown as [5, 3]), the neighborhood encompasses $5 \times 5 \times 3 = 75$ grid boxes. The treatment of neighborhood data depended on the selected fuzzy method and included for example, averaging, thresholding, or the generation of empirical frequency distributions (Lockhoff *et al.*, 2014). As proposed by Lockhoff et al. (2014), fractions skill score (FSS) was chosen for the fuzzy method and was determined as follows:

$$FSS = 1 - \frac{\sum_N (\langle P_{3B42}\rangle_s - \langle P_{RG}\rangle_s)^2}{\sum_N \langle P_{3B42}\rangle_s^2 + \sum_N \langle P_{3B42}\rangle_s^2} \qquad (6)$$

where $\langle P_{3B42}\rangle$ and $\langle P_{RG}\rangle$ are the fraction of grid boxes in a neighborhood with extreme events observed by 3B42 and RG, respectively, N is the number of neighborhood in the domain considered, and $\langle \quad \rangle_s$ indicate that the fractions are calculated based on the neighborhood surrounding the grid box of interest for the indicated spatiotemporal scale. FSS is calculated per grid box, so that the FSS is calculated for the temporal domain (i.e. the time period covered). Therefore, N is equal to the number of days per season for 15 years. The FSS ranges between 0 and 1 with 1 indicating the perfect score. The value of FSS above which the assessed dataset is considered to have useful (better than random) skill is given by:

$$FSS_{usefull} = 0.5 + \frac{f_y}{2} \tag{7}$$

where f_y is the domain average fraction observed by the reference dataset (Roberts and Lean 2008); that is, here the average fraction of extreme events observed by RG at a specific grid point over the entire time period.

Extreme thresholds were calculated per grid box at a 0.25° resolution. The extreme thresholds were averaged over the increased spatial neighborhood. As the size of the neighborhood increased, the neighborhood window crossed the borders of the study area; therefore, it included no-data values. Thus, a neighborhood was scrutinized only when at least 50% of the neighborhood grid boxes provided valid values. This led to a decrease in the size of the area along the borders with increasing spatial scale.

4. Results

4.1. Climatological statistics

Before investigating the extreme indices, based upon 15 years (2000-2014) of daily rainfall estimates, total rainfall (TOT), number of wet days (NWD), and wet day intensity (INT) were calculated for 3B42 and RG at seasonal time scales and different years. Qualitatively, Figure

5 shows that the spatial patterns compared TOT with NWD satisfactorily. The north and northwest regions of the province had the highest values, while the southern and southeast grid cells of the province had the lowest values. However, the spatial distribution of INT in the southeastern regions based on 3B42 did not correspond to the results of RG, suggesting that it might be due to underestimation of NWD in these regions. According to BR maps, 3B42 underestimated NWD (88% of the grid cells). Pierre *et al*. (2011) also reported underestimation of NWD by 3B42 in Sahelian belt, Africa. Correlation (r) between 3B42 and RG results decreased for TOT, INT and NWD, respectively. Buarque *et al*. (2011) also reported a higher correlation for estimation of TOT than NWD by 3B42 in the Amazon region.

As shown in Table 3, the mean test results indicated that the NWD had the highest number of grid cells with different means at probability level of 5%. However, the magnitude of results was not the same at different time scales, so that it was the highest for winter season. This might be due to higher number of precipitation events in this season. Furthermore, the most insignificant percentage of means was obtained for TOT. On the other hand, Levene and F tests showed that the highest percentage of grid cells with different variances were related to INT except for the Levene test in autumn, which identified NWD with the highest percentage of significant difference.

4.2. R10mm and Rx1Day

The means of R10mm and Rx1Day obtained by 3B42 and RG datasets across Fars province for the period 2000-2014 along with the corresponding spatial distributions of BR and r are indicated in Figure 6. The means of the aforementioned indices calculated from RG and 3B42 datasets were almost identical for spatial variation, and so were they with respect to the minimum of estimated R10mm; nonetheless, the same indices calculated from 3B42 dataset indicated more grid cells with the minimum range (2.1 – 4 days) in south and eastern parts of the study area. With respect to BR map, 3B42 underestimated R10mm in over 81% of the grid cells. The rate of underestimation decreased in other seasons. As shown in Table 1, the average BR across the studied region was 1.02 for spring and autumn. Contrary to R10mm, overestimation was predominant in the Rx1day, so that the BR mean for spring and autumn winter seasons were 1.16, 1.08 and 1.3, respectively (Table 4.). Regarding the correlation coefficient (Figure 6), in 63% and 81% of grid cells for R10mm and in 38% and 65% of grid cells for Rx1Day, the correlation coefficient was greater than 0.7 and 0.6, respectively. This shows a better accordance for the estimated values of R10mm than Rx1Day. Similar results were obtained for spring and autumn. As shown in Table 4, the spatially averaged values of r for R10mm were higher than those for Rx1Day.

Table 4 depicts MW and t test results. The maximum difference between the means of Rx1Day and R10mm indices calculated from 3B42 and RG was observed in the winter (i.e., 12% of the grid cells). In other seasons (spring and autumn), a better match was found between the results. Thus, overall, the consistency between the means of the aforementioned indices was very good. As to the equal variance tests, except for F test in winter, which indicated a significant difference for Rx1Day in 28% of grid cells, the results of other parametric and non-parametric equal variance tests were satisfactory in all seasons for both of the EPIs.

4.2. Percentile indices

As shown in Figures 7 and 8, the R95pTOT and total number of days with precipitation higher than Q95 (R95pDay) values were computed to compare the amount and frequency of determined extreme events by 3B42 and RG datasets. Then, fuzzy analysis was employed to compare the ability of this index to predict the occurrence of precipitation amounts higher than Q95 in different temporal and spatial neighbors (Figure 9). Finally, the improved index RS95pTOT was indicated in Figure 10.

As shown in Figure 7, the spatial distribution of R95pTOT obtained by 3B42 and RG overlapped in the margins of Fars province. However, 3B42 results depicted a zone with high values of extremes in central parts of the province. A similar difference in spatial pattern of 3B42 and RG results was also observed in Figure 8 for the R95pDay. According to the BR maps (Figures 7 and 8), it is obvious that 3B42 overestimated R95pTOT (R95pDay) in 70(63) % of grid cells, as the spatial average value of BR was 1.3 (1.17).

Average values of r for R95pTOT (0.76) and R95pDay (0.71) confirm that good correlations existed between the results of RG and 3B42 in winter; however, the r values were lower in south-eastern parts of Fars, where lower amount and frequency of precipitation exists. With a similar spatial pattern (results are not shown), the average r for R95pTOT (R95pDay) decreased to 0.52 (0.53) and 0.36 (0.36) in the spring and autumn seasons, respectively, indicating a decrease in the matching of 3B42 and RG results in seasons with decreased precipitation totals. Mann-Whitney and t-tests showed no significant difference between the means of R95pTOT by 3B42 and RG for R95pTOT in 92 and 98% of grid cells for winter, 99 % of the grid cells for spring and 99 and 98% of grid cells for autumn, respectively, at 5% significance level. Furthermore, F and Levene tests showed no significant difference between the variance of R95pTOT obtained by the two datasets in 97 and 92% of grid cells for winter, 82 and 79% of grid cells for spring and 75 and 79% of grid cells for autumn, respectively, at 5% significance level. The matching percentage of the mean and variance tests for the R95pDay index was equal to or slightly higher than the R95pTOT ones. Therefore, it is concluded that there was a very good accordance between means and variances of the obtained 95 percentile extremes by RG and 3B42.

As shown in Figure 9, the 95th percentile threshold was used to define extreme events with reference to temporal and spatial neighborhood sizes for winter. The [1, 1] time-scale pair (i.e. The former indicates the temporal neighborhood size in days, the latter the spatial neighborhood in pixels) is a substitute for the traditional point-by-point verification, which results in low FSS values. The objective was to mitigate the effect of mismatches due to sampling and difference in the definition of the pair. The objective is achieved with a steady increase in FSS to values above the local FSS_{useful}, assigning 3B42 a useful skill at the aforementioned scales. As Figure 9 indicates, the improvement of results due to increasing spatial neighborhood was greater than the increasing temporal neighborhood, so that for all the temporal neighborhoods, when the spatial neighborhood increased from 1 pixel to 3 pixels, the percentage of grid boxes with FSS higher than FSS_{useful} almost doubled. In all combinations of time and space, the southeastern part of province had the lowest values of FSS, even at the scale [7, 7], the pixels in this area had FSS less than FSS_{useful}. The phenomenon may be due to the scarcity of wet days in this area (Figure 5). The same spatial patterns were observed in other seasons as well. However, the percentages of grid cells with useful estimations were lower than those in winter. For example, for spring and autumn at

[1,1] ([7,7]), the percentages of grid cells with useful estimations were 15% (87%) and 5% (79%), respectively.

As explained in Section 2.3.1, RS95pTOT was calculated for each grid cell and season. To be eligible, there must be ten or more precipitation events per season. As Figure 5 shows, the number of eligible years increased from the low rainfall areas in the south-east to northwest areas with highest precipitation totals. Regarding the BR map, in more than 58 percent of the grid cells, 3B42 underestimated the RS95pTOT. The mean BR was 0.98 for the whole province. These were in contrast to the R95pTOT results, where 3B42 overestimated R95pTOT in most locations. Also, except for the eastern regions, the spatial consistency of the RS95pTOT was much higher than that of the R95pTOT.

4.3. Dry/wet spells

In this section, first the results of 3B42 and RG in the estimation of CWD and CDD indices is compared. Then, given the uncertainties for the estimation from RG data, the distribution of TGD is fitted to the number of WP durations in each season. Finally, the average value and the 95th percentile (WPs_mean and WPs_P95, respectively) of the fitted distribution is compared from both RG and 3B42 datasets.

As can be observed in Figure 11, the spatial distributions of obtained CDD and CWD by RG and 3B42 datasets overlapped, so that high values of duration indices were observed in northern parts and the low values were located in southern parts of Fars province. It was shown in section 4.1 that 3B42 generally underestimated NWD. A similar trend was observed for CWD in Figure 11, so that the BR value for this parameter was less than 1 in more than

89% of the grid cells. Consequently, the CDD values were overestimated by 3B42 in 84% of grid cells. On the other hand, the average r for CWD and CDD (0.23 and 0.39, respectively) showed a low correlation between the results of RG and 3B42. Parametric and nonparametric tests, namely, t-test and Mann-Whitney, respectively, showed that for CDD (CWD) in 93 (39) and 90 (39) % of the grid cells, there was no significant difference between results of 3B42 and RG datasets at 5% significance level. Levene and F tests showed that in 96 (80) and 91 (75)% of the grid cells , respectively, no significant difference was observed between the variances of obtained CDD (CWD) by 3B42 and RG, at 5% significance level.

Because the number of rainy events in the April-September season was low in most of grid cells, it was not possible to fit TGD to these data. As a result, April-September data were excluded from TGD analysis. The area under investigation is a semi-arid region and has a long duration of dry spells, even in the wet season. This means a large value for N in Equation 5, which resulted in lengthening time for fitting method proposed by Zolina *et al.* (2013). Therefore, obtaining TGD function for DPs data was discarded due to hardware constraints and only TGD distribution calculations were performed for wet spells of the wet season (October-March).

Regarding WPs_mean and WPs_P95 in the wet season, Figure 12 shows that 3B42 underestimated them in 98 and 89% of the grid cells, respectively, which was similar to CWD results. The spatially averaged values of r for these two parameters were 0.29 and 0.23, respectively, which showed a low correlation between the results of 3B42 and RG. It can be concluded that the use of TGD did not increase the correlation between 3B42 and RG. On the other hand, the use of TGD did not change the rate of underestimation/overestimation of extreme wet spells significantly.

4.3. Case studies

For more detailed comparison between 3B42 and RG results, two grid cells- one with the highest annual rainfall (30.375^{o}N, 51.875^{o}E) and the other in the low rainfall regions of southeast of the province (27.875^{o}N, 54.375^{o}E)- were selected. Initially, the time series of winter rainfall were plotted for each location based on RG and 3B42 (Figure 13). Then empirical and TGD histograms of WPs were compared in Figure 14.

The first interesting point in Figure 13 is that the Q95 value at point 15 and 140 was under- and overestimated by 3B42, respectively. This is not related to under/over estimation of total rainfall, so that BR values for the total rainfall in these grid cells were 0.86 and 0.83, respectively. The underestimation of wet days at 140 (BR= 0.72) caused the overestimation of extreme rainfall. Regarding grid cell 15, the opposite is true because the BR value for the NWD was 1.15, Therefore, Q95 was underestimated by 3B42. The interesting point in this figure is that although the R95pTOT had a good correlation coefficient with the precipitation data of rain gauges, the time for the maximum amount of rainfall in the time series had no adaptation in both locations, so that for grid cell No. 15, the maximum daily rainfall was observed in 2002 and 2004 based on RG and 3B42, respectively. This trend also took place at grid cell No. 140, which as RG and 3B42 indicated received the maximum daily rainfall in 2009 and 2006, respectively. Another interesting point is that, regardless of the over/underestimation of Q95, 3B42 overestimated the maximum daily precipitation during the time series. This trend was observed in 77% of the examined grid cells.

The empirical histograms of wet durations and approximation of these histograms by the TGD for grid cell No. 15 and 140 are indicated in Figure 14. These histograms were obtained from annual time series of WPs in wet seasons. For all WPs, the probability of experimental and the TGD histograms were close to each other except for 1 and 2 days durations at grid cell No. 140. At this location, the WPs frequency with 2 days duration was the highest. A phenomenon that resulted in diffraction of the two histograms based on RG results. As 3B42 showed, the aforementioned cell received the highest frequency in one-day rainfall, confirming the fact that this region was the rainiest region of the province; therefore, this result is not unexpected. Regarding grid cell No. 140, there was a good agreement between the probabilities of TGD and experimental histograms obtained by RG and 3B42.

5. Discussion

The overall results show that the spatial distribution of extreme indices by 3B42 overlapped with the results of RG. Nastos *et al*. (2013) showed that high altitudes have increased values of percentile and threshold EPIs compared to coastal regions. According to Nastos *et al.* (2013), in mountainous regions of the north-western part of Fars higher values of extreme measures were observed compared to southeast parts of the province. Furthermore, the results showed that generally a higher correlation between the results of RG and 3B42 was observed in these regions. The previous studies also documented that there was a high correlation coefficient between RG and 3B42 monthly precipitation over the regions with high amounts of precipitation (Shirvani and Fakharizade-Shirazi, 2014; Javnmard *et al*., 2010; Moazami *et al*., 2016). Among the ETCCDI indices, R95pTOT and Rx1Day had the highest correlation coefficients, while CDD indices had the lowest values with the precipitation data of rain gauges. According to Moazami *et al*. (2016) the average value of correlation coefficient between 3B42 precipitation and synoptic rain gauges across Iran is 0.61. Shirvani and Fakharizade-Shirazi (2014) showed that the range of correlation coefficient between the precipitation data of rain gauges and 3B42 was between 0.1-0.7 over Fars province for the period 1998-2011. However, the maximum value of r across the region for R10mm, CWD, CDD, R95pTOT, R95pDay, and Rx1Day were 0.96, 0.86, 0.91, 0.97, 0.95, and 0.92 in the current study. This shows that the best obtained values of correlation coefficient for precipitation extreme values were higher than those obtained for precipitation data across the area under investigation. Although the researchers presented the results in separate seasons, their findings are also confirmed when mean values of r for annual scale (not shown in the results) for R10mm, CWD, R95pTOT, R95pDay, Rx1Day, which are 0.66, 0.66, 0.80, and 0.63 respectively, are compared with the results reported by Moazami *et al*. (2016) in Iran. A probable reason for increased correlation coefficient is that R10mm, CWD, R95pTOT, R95pDay, Rx1Day obtained from seasonal rainfall data and certain date of extreme rainfall occurrence is not a matter of concern in determination of them. This is confirmed when the correlation coefficient of total seasonal rainfall is considered (Figure 5), which was higher than 0.8 for most of the area under investigation.

Results from 3B42 indicate that generally R10mm and CWD are underestimated, whereas CDD, R95pDay, R95pTOT and Rx1Day indices are overestimated. Due to lower relative humidity and higher temperature in semi-arid zones, rain drops may evaporate before reaching the earth surface (Tesfagiorgis *et al*. 2011). Shirvani and Fakhari Zade Shirazi (2014) show that in north-western part of Fars province- with higher precipitation and altitudes - underestimations of precipitation are observed, whereas in eastern parts- with lower precipitation and altitudes- overestimation of precipitation are observed. Accordingly, overestimation of R10mm, and percentile indices in southeastern parts of the province could be justified. However, in the mountainous regions, where the distance of raindrop travel to earth is shorter, overestimations of these extreme are observed. This is also consistent with the results reported by Moazami *et al*. (2016) for Iran.

To evaluate the prediction of extreme precipitation events by 3B42, a fuzzy method was used. The results showed a better performance for the satellite at the regions with higher amounts of rainfall. Lockhoff *et al*. (2014) used the same method for the evaluation of GPCP 90th percentile threshold over Europe. They showed that at [1, 1] (1 pixel and 1 day window), none of GPCP grid cells had the value of FSS higher than FSS_{useful}. However, in the present study, 20% of grid cells had the FSS value higher than the criteria, despite the facts that pixel size for 3B42 is one fourth of GPCP and the threshold value for extreme precipitation (Q90) in their study was lower than Q95. AghaKouchak *et al*., (2011) and Lockhoff *et al*., (2014) indicated that prediction of detection of precipitation extremes by satellite products decreased as the extreme threshold value increased from Q75 to Q95, which confirms a better performance of 3B42 as compared to GPCP products. The researchers also compared the daily precipitation estimates of 3B42 and GPCP results with each other (not shown), and found a better performance of 3B42.

The index R95pTOT shows the relative contribution of very wet days (i.e. days with precipitation amounts exceeding the 95th percentile) to the total precipitation amounts. This index has often been used to monitor the changes of extreme precipitation amounts. However, the use of this index has been questioned because of its strong year-to-year variations (Zolina *et al.*, 2009; Leander *et al.*, 2014). Leander *et al.*, 2014 showed that R95pTOT is influenced by changes in the mean wet-day precipitation. Since the problem is a matter of concern in trend analysis of extreme precipitation, the researchers also compared the results of 3B42 and RG in estimation of the improved index RS95pTOT. The results showed that the spatial consistency between the 3B42 and RG results was very high especially in the north and west parts of Fars with higher values and frequencies of precipitation. The main problem in the estimation of RS95pTOT was that a minimum number of days with precipitation (i.e. 10 days) were required. This criterion reduced the eligible years for calculation of RS95pTOT to zero in some south-eastern grid cells of Fars. This makes trend analysis impossible with this extreme index in arid zones. However, this problem was not observed in the northwestern parts of the study area.

Any comprehensive analysis of wet/dry durations and extreme precipitation is made possible only when special attention is paid to the extent of data coverage and individual records. In effect, it means that dense precipitation networks are required for such an analysis (Zolina *et al*., 2009 and 2013). The density of rain gauges in a region is a function of the frequency and the intensity of precipitation. Since southern parts of Fars receive low rainfall, the researchers believe that their findings suffer from low rain gauges density problem. This problem is most noticeable in the northeastern part of the study area. Hence, the findings are most robust for grid cells that include at least one rain gauge.

6. Conclusion

Research on extreme climate characteristics makes it possible to reveal the spatial and temporal features of a region in the extremeness of precipitation events. In this study, EPIs were obtained from high density rain gauges and TRMM (3B42 V7) datasets. The spatial consistency of 3B42 and RG was good, so that they worked equally well in the northwestern parts of Fars with higher extreme precipitation frequency and amounts. The fuzzy evaluation of results revealed that 3B42 estimations of extreme conditions were useful only in 20% of grid cells on certain days. This was a better result for a satellite product than the previous studies. The fuzzy results got better, as the window of temporal or spatial neighborhood were extended. An interesting conclusion for the results was that the effect of increasing spatial neighborhood was significantly higher than that of extending temporal window. The percentile precipitation was also obtained based on Weibull distribution to eliminate the seasonal changes of rainfall averages uncertainty. Although the consistency of 3B42 and RG results was very good in northwestern parts of Fars, due to lack of required number of wet days in southern parts, the results of this method could not be derived in most of the seasons. This was the main disadvantage of this method in the semi-arid region Fars. For duration indices, another probabilistic method was used based on truncated geometric distribution to remove the uncertainty of probable missing rainfall data. The results indicated that although the consistency between 3B42 and RG datasets was very good, it did not increase significantly in general with the application of the method. It is noteworthy that the correlation between the results of the two datasets was acceptable and higher than those obtained in previous studies for evaluating TRMM precipitation data over Fars province and Iran. Therefore, with respect to obtained bias ratios for the indices, calibration approaches are recommended to improve satellite results in climate studies.

Acknowledgements

The researchers thank the Fars Regional Water Organization for providing precipitation data used in this study. They also appreciate the anonymous reviewers who have taken out time to read this manuscript and given them very useful feedbacks. Their critical review improved the clarity and quality of this paper.

Supporting Information

The following supporting information is available as part of online article:

Table S1. List of Meteorological rain gauge stations along with their geographic characteristics and statistics for the respective annual precipitation in period 2000 to 2014.

7. References

1. AghaKouchak, A., Behrangi, A., Sorooshian, S., Hsu, K., & Amitai, E. (2011). Evaluation of satellite-retrieved extreme precipitation rates across the central United

States. *Journal of Geophysical Research: Atmospheres*, *116*(D2). https://doi.org/10.1029/2010JD014741.

2. Alijanian, M., Rakhshandehroo, G. R., Mishra, A. K., & Dehghani, M. (2017). Evaluation of satellite rainfall climatology using CMORPH, PERSIANN-CDR, PERSIANN, TRMM, MSWEP over Iran. *International Journal of Climatology*, *37*(14), 4896-4914. https://doi.org/10.1002/joc.5131.
3. Ashouri, H., Hsu, K. L., Sorooshian, S., Braithwaite, D. K., Knapp, K. R., Cecil, L. D., ... & Prat, O. P. (2015). PERSIANN-CDR: Daily precipitation climate data record from multisatellite observations for hydrological and climate studies. *Bulletin of the American Meteorological Society*, *96*(1), 69-83. https://doi.org/10.1175/BAMS-D-13-00068.1.
4. Awange, J. L., Ferreira, V. G., Forootan, E., Andam-Akorful, S. A., Agutu, N. O., & He, X. F. (2016). Uncertainties in remotely sensed precipitation data over Africa. *International Journal of Climatology*, *36*(1), 303-323. https://doi.org/10.1002/joc.4346.
5. Azadi, S., & Karimi-Jashni, A. (2016). Verifying the performance of artificial neural network and multiple linear regression in predicting the mean seasonal municipal solid waste generation rate: A case study of Fars province, Iran. *Waste Management*, *48*, 14-23. https://doi.org/10.1016/j.wasman.2015.09.034.
6. Bharti, V., Singh, C., Ettema, J., & Turkington, T. A. R. (2016). Spatiotemporal characteristics of extreme rainfall events over the Northwest Himalaya using satellite

data. *International journal of climatology*, *36*(12), 3949-3962. https://doi.org/10.1002/joc.4605.

7. Buarque, D. C., de Paiva, R. C. D., Clarke, R. T., & Mendes, C. A. B. (2011). A comparison of Amazon rainfall characteristics derived from TRMM, CMORPH and the Brazilian national rain gauge network. *Journal of Geophysical Research: Atmospheres*, *116*(D19). https://doi.org/10.1029/2011JD016060
8. Cai, Y., Jin, C., Wang, A., Guan, D., Wu, J., Yuan, F., & Xu, L. (2016). Comprehensive precipitation evaluation of TRMM 3B42 with dense rain gauge networks in a mid-latitude basin, northeast, China. *Theoretical and applied climatology*, *126*(3-4), 659-671.https://doi.org/10.1007/s00704-015-1598-4.
9. Chen, S., Hong, Y., Gourley, J. J., Huffman, G. J., Tian, Y., Cao, Q., ... & Li, Z. (2013). Evaluation of the successive V6 and V7 TRMM multisatellite precipitation analysis over the Continental United States. *Water Resources Research*, *49*(12), 8174-8186. https://doi.org/ 10.1002/2012WR012795.
10. Ebert, E. E. (2008). Fuzzy verification of high-resolution gridded forecasts: a review and proposed framework. *Meteorological applications*, *15*(1), 51-64. https://doi.org/10.1002/met.25.
11. Groisman, P. Y., & Knight, R. W. (2008). Prolonged dry episodes over the conterminous United States: new tendencies emerging during the last 40 years. *Journal of Climate*, *21*(9), 1850-1862. https://doi.org/10.1175/2007JCLI2013.1.
12. Hajani, E., & Rahman, A. (2018). Characterizing changes in rainfall: a case study for New South Wales, Australia. *International Journal of Climatology*, *38*(3), 1452-1462. https://doi.org/10.1002/joc.5258

13. Haylock, M. R., Hofstra, N., Klein Tank, A. M. G., Klok, E. J., Jones, P. D., & New, M. (2008). A European daily high-resolution gridded data set of surface temperature and precipitation for 1950–2006. *Journal of Geophysical Research: Atmospheres*, *113*(D20). https://doi.org/10.1029/2008JD010201.

14. Heidinger, H., Carvalho, L., Jones, C., Posadas, A., & Quiroz, R. (2018). A new assessment in total and extreme rainfall trends over central and southern Peruvian Andes during 1965–2010. *International Journal of Climatology*, *38*, e998-e1015. https://doi.org/10.1002/joc.5427.

15. Hong, Y., Gochis, D., Cheng, J. T., Hsu, K. L., & Sorooshian, S. (2007). Evaluation of PERSIANN-CCS rainfall measurement using the NAME event rain gauge network. *Journal of Hydrometeorology*, *8*(3), 469-482. https://doi.org/ 10.1175/JHM574.1.

16. Hsu, K. L., Gao, X., Sorooshian, S., & Gupta, H. V. (1997). Precipitation estimation from remotely sensed information using artificial neural networks. *Journal of Applied Meteorology*, *36*(9), 1176-1190. https://doi.org/ 10.1175/1520-0450(1997)036<1176:PEFRSI>2.0.CO;2.

17. Huffman, G. J., Adler, R. F., Morrissey, M. M., Bolvin, D. T., Curtis, S., Joyce, R., ... & Susskind, J. (2001). Global precipitation at one-degree daily resolution from multisatellite observations. *Journal of hydrometeorology*, *2*(1), 36-50. https://doi.org/ 10.1175/1525-7541(2001)002<0036:GPAODD>2.0.CO;2.

18. Huffman, G. J., Bolvin, D. T., Nelkin, E. J., Wolff, D. B., Adler, R. F., Gu, G., ... & Stocker, E. F. (2007). The TRMM multisatellite precipitation analysis (TMPA):

Quasi-global, multiyear, combined-sensor precipitation estimates at fine scales. *Journal of hydrometeorology*, *8*(1), 38-55. https://doi.org/ 10.1175/JHM560.1.

19. James, G., Witten, D., Hastie, T., & Tibshirani, R. (2013). *An introduction to statistical learning* (Vol. 112). New York: springer.
20. Javanmard, S., Yatagai, A., Nodzu, M. I., BodaghJamali, J., & Kawamoto, H. (2010). Comparing high-resolution gridded precipitation data with satellite rainfall estimates of TRMM_3B42 over Iran. *Advances in Geosciences*, *25*, 119-125. https://doi.org/10.5194/adgeo-25-119-2010.
21. Joyce, R. J., Janowiak, J. E., Arkin, P. A., & Xie, P. (2004). CMORPH: A method that produces global precipitation estimates from passive microwave and infrared data at high spatial and temporal resolution. *Journal of Hydrometeorology*, *5*(3), 487-503. https://doi.org/ 10.1175/1525-7541(2004)005<0487:CAMTPG>2.0.CO;2.
22. Katiraie-Boroujerdy, P. S., Ashouri, H., Hsu, K. L., & Sorooshian, S. (2017). Trends of precipitation extreme indices over a subtropical semi-arid area using PERSIANN-CDR. *Theoretical and Applied Climatology*, *130*(1-2), 249-260. https://doi.org/10.1007/s00704-016-1884-9.
23. Klein Tank, A. M. G., & Können, G. P. (2003). Trends in indices of daily temperature and precipitation extremes in Europe, 1946–99. *Journal of climate*, *16*(22), 3665-3680. https://doi.org/10.1175/1520-0442(2003)016<3665:TIIODT>2.0.CO;2
24. Leander, R., Buishand, T. A., & Tank, A. K. (2014). An alternative index for the contribution of precipitation on very wet days to the total precipitation. *Journal of Climate*, *27*(4), 1365-1378. https://doi.org/10.1175/JCLI-D-13-00144.1.

25. Li, X., Wang, X., & Babovic, V. (2018). Analysis of variability and trends of precipitation extremes in Singapore during 1980–2013. *International Journal of Climatology*, *38*(1), 125-141. https://doi.org/10.1002/joc.5165

26. Lockhoff, M., Zolina, O., Simmer, C., & Schulz, J. (2014). Evaluation of satellite-retrieved extreme precipitation over Europe using gauge observations. *Journal of Climate*, *27*(2), 607-623. https://doi.org/10.1175/JCLI-D-13-00194.1.

27. Manz, B., Páez-Bimos, S., Horna, N., Buytaert, W., Ochoa-Tocachi, B., Lavado-Casimiro, W., & Willems, B. (2017). Comparative Ground Validation of IMERG and TMPA at Variable Spatiotemporal Scales in the Tropical Andes. *Journal of Hydrometeorology*, *18*(9), 2469-2489. https://doi.org/10.1175/JHM-D-16-0277.1

28. McCuen, R. H. (2016). *Hydrologic analysis and design* (Vol. 3). Prentice Hall.

29. Moazami, S., Golian, S., Hong, Y., Sheng, C., & Kavianpour, M. R. (2016). Comprehensive evaluation of four high-resolution satellite precipitation products under diverse climate conditions in Iran. *Hydrological Sciences Journal*, *61*(2), 420-440. https://doi.org/10.1080/02626667.2014.987675.

30. Najafi, M. R., & Moazami, S. (2016). Trends in total precipitation and magnitude–frequency of extreme precipitation in Iran, 1969–2009. *International Journal of Climatology*, *36*(4), 1863-1872. https://doi.org/10.1002/joc.4465.

31. Nastos, P. T., Kapsomenakis, J., & Douvis, K. C. (2013). Analysis of precipitation extremes based on satellite and high-resolution gridded data set over Mediterranean basin. *Atmospheric Research*, *131*, 46-59. https://doi.org/10.1016/j.atmosres.2013.04.009.

32. Nastos, P. T., Kapsomenakis, J., & Philandras, K. M. (2016). Evaluation of the TRMM 3B43 gridded precipitation estimates over Greece. *Atmospheric Research*, *169*, 497-514. https://doi.org/10.1016/j.atmosres.2015.08.008.

33. Nordstokke, D. W., Zumbo, B. D., Cairns, S. L., & Saklofske, D. H. (2011). The operating characteristics of the nonparametric Levene test for equal variances with assessment and evaluation data. *Practical Assessment, Research & Evaluation*, *16*. Available online: http://pareonline.net/getvn.asp?v=16&n=5.

34. Ouma, Y. O., Owiti, T., Kipkorir, E., Kibiiy, J., & Tateishi, R. (2012). Multitemporal comparative analysis of TRMM-3B42 satellite-estimated rainfall with surface gauge data at basin scales: daily, decadal and monthly evaluations. *International journal of remote sensing*, *33*(24), 7662-7684. https://doi.org/10.1080/01431161.2012.701347.

35. Pierre, C., Bergametti, G., Marticorena, B., Mougin, E., Lebel, T., & Ali, A. (2011). Pluriannual comparisons of satellite-based rainfall products over the Sahelian belt for seasonal vegetation modeling. *Journal of Geophysical Research: Atmospheres*, *116*(D18). https://doi.org/10.1029/2011JD016115

36. Pombo, S., & de Oliveira, R. P. (2015). Evaluation of extreme precipitation estimates from TRMM in Angola. *Journal of Hydrology*, *523*, 663-679. https://doi.org/10.1016/j.jhydrol.2015.02.014.

37. Prakash, S., Mitra, A. K., Gairola, R. M., Norouzi, H., & Pai, D. S. (2018). Status of High-Resolution Multisatellite Precipitation Products Across India. In *Remote Sensing of Aerosols, Clouds, and Precipitation* (pp. 301-314). https://doi.org/10.1016/B978-0-12-810437-8.00014-1.

38. Prakash, S., Mitra, A. K., Pai, D. S., & AghaKouchak, A. (2016a). From TRMM to GPM: How well can heavy rainfall be detected from space?. *Advances in Water Resources*, *88*, 1-7. http://dx.doi.org/10.1016/j.advwatres.2015.11.008.

39. Prakash, S., Mitra, A. K., Rajagopal, E. N., & Pai, D. S. (2016b). Assessment of TRMM-based TMPA-3B42 and GSMaP precipitation products over India for the peak southwest monsoon season. *International Journal of Climatology*, *36*(4), 1614-1631. https://doi.org/10.1002/joc.4446.

40. Prat, O. P., & Nelson, B. R. (2014). Characteristics of annual, seasonal, and diurnal precipitation in the Southeastern United States derived from long-term remotely sensed data. *Atmospheric research*, *144*, 4-20. https://doi.org/10.1016/j.atmosres.2013.07.022.

41. Qiao, L., Hong, Y., Chen, S., Zou, C. B., Gourley, J. J., & Yong, B. (2014). Performance assessment of the successive Version 6 and Version 7 TMPA products over the climate-transitional zone in the southern Great Plains, USA. *Journal of hydrology*, *513*, 446-456. https://doi.org/10.1016/j.jhydrol.2014.03.040.

42. Raveh-Rubin, S., & Wernli, H. (2015). Large-scale wind and precipitation extremes in the Mediterranean: a climatological analysis for 1979–2012. *Quarterly Journal of the Royal Meteorological Society*, *141*(691), 2404-2417. https://doi.org/10.1002/qj.2531.

43. Raziei, T., Mofidi, A., Santos, J. A., & Bordi, I. (2012). Spatial patterns and regimes of daily precipitation in Iran in relation to large-scale atmospheric circulation. *International Journal of Climatology*, *32*(8), 1226-1237. https://doi.org/10.1002/joc.2347

44. Roberts, N. M., & Lean, H. W. (2008). Scale-selective verification of rainfall accumulations from high-resolution forecasts of convective events. *Monthly Weather Review*, *136*(1), 78-97. https://doi.org/10.1175/2007MWR2123.1.

45. Shirvani, A., & Fakhari Zade Shirazi E. (2014). Comparison of ground based observation of precipitation with satellite estimations in Fars province. *Journal Agricultural. Meteorology*. 2: 1-15 (in Persian).

46. Shrestha, A. B., Bajracharya, S. R., Sharma, A. R., Duo, C., & Kulkarni, A. (2017). Observed trends and changes in daily temperature and precipitation extremes over the Koshi river basin 1975–2010. *International Journal of Climatology*, *37*(2), 1066-1083. https://doi.org/10.1002/joc.4761.

47. Skofronick-Jackson, G., Petersen, W. A., Berg, W., Kidd, C., Stocker, E. F., Kirschbaum, D. B., & Kirstetter, P. E. (2017). The global precipitation measurement (GPM) mission for science and society. *Bulletin of the American Meteorological Society*, *98*(8), 1679-1695. https://doi.org/10.1175/BAMS-D-15-00306.1.

48. Snedecor, G. W. C., & William, G. (1989). *STATISTICAL METHODS/GEORGE W. SNEDECOR AND WILLIAM G. COCHRAN* (No. QA276. 12. S6313 1989.).

49. Soufi, M. (2004, July). Morpho-climatic classification of gullies in Fars province, Southwest of IR Iran. In *International Soil Conservation Organisation Conference, Brisbane* (p. 4).

50. Stedinger, J. R. (1993). Frequency analysis of extreme events. *in Handbook of Hydrology.*

51. Tangang, F., Juneng, L., & Aldrian, E. (2017). Observed changes in extreme temperature and precipitation over Indonesia. *International Journal of Climatology, 37*(4), 1979-1997. https://doi.org/10.1002/joc.4829.

52. Tarek, M. H., Hassan, A., Bhattacharjee, J., Choudhury, S. H., & Badruzzaman, A. B. M. (2017). Assessment of TRMM data for precipitation measurement in Bangladesh. *Meteorological Applications*, *24*(3), 349-359. https://doi.org/10.1002/met.1633.

53. Tesfagiorgis, K., Mahani, S. E., Krakauer, N. Y., & Khanbilvardi, R. (2011). Bias correction of satellite rainfall estimates using a radar-gauge product-a case study in Oklahoma (USA). *Hydrology and Earth System Sciences*, *15*(8), 2631. https://doi.org/10.5194/hess-15-2631-2011.

54. Ushio, T., Sasashige, K., Kubota, T., Shige, S., Okamoto, K. I., Aonashi, K., ... & Oki, R. (2009). A Kalman filter approach to the Global Satellite Mapping of Precipitation (GSMaP) from combined passive microwave and infrared radiometric data. *Journal of the Meteorological Society of Japan. Ser. II*, *87*, 137-151. https://doi.org/10.2151/jmsj. 87A.

55. Wang, F., Yang, S., Higgins, W., Li, Q., & Zuo, Z. (2014). Long-term changes in total and extreme precipitation over China and the United States and their links to oceanic–atmospheric features. *International Journal of Climatology*, *34*(2), 286-302. https://doi.org/10.1002/joc.3685.

56. Webster, R., & Oliver, M. A. (2007). *Geostatistics for environmental scientists*. John Wiley & Sons.

57. Wehbe, Y., Ghebreyesus, D., Temimi, M., Milewski, A., & Al Mandous, A. (2017). Assessment of the consistency among global precipitation products over the United Arab Emirates. *Journal of Hydrology: Regional Studies*, *12*, 122-135. https://doi.org/10.1016/j.ejrh.2017.05.002.

58. Wilks, D. S. (2011). Statistical methods in the atmospheric sciences (Vol. 100). Academic press.

59. Zhang, X., Alexander, L., Hegerl, G. C., Jones, P., Tank, A. K., Peterson, T. C., ... & Zwiers, F. W. (2011). Indices for monitoring changes in extremes based on daily temperature and precipitation data. *Wiley Interdisciplinary Reviews: Climate Change*, *2*(6), 851-870. https://doi.org/10.1002/wcc.147.

60. Zhao, T., & Yatagai, A. (2014). Evaluation of TRMM 3B42 product using a new gauge-based analysis of daily precipitation over China. *International Journal of Climatology*, *34*(8), 2749-2762. https://doi.org/10.1002/joc.3872.

61. Zhao, Y., Xie, Q., Lu, Y., & Hu, B. (2017). Hydrologic Evaluation of TRMM Multisatellite Precipitation Analysis for Nanliu River Basin in Humid Southwestern China. *Scientific Reports*, *7*(1), 2470. https://doi.org/10.1038/s41598-017-02704-1.

62. Zolina, O., Kapala, A., Simmer, C., & Gulev, S. K. (2004). Analysis of extreme precipitation over Europe from different reanalyses: a comparative assessment. Global and Planetary Change, 44(1-4), 129-161. https://doi.org/10.1016/j.gloplacha.2004.06.009.

63. Zolina, O., Simmer, C., Belyaev, K., Gulev, S. K., & Koltermann, P. (2013). Changes in the duration of European wet and dry spells during the last 60 years. Journal of Climate, 26(6), 2022-2047. https://doi.org/10.1175/JCLI-D-11-00498.1.

64. Zolina, O., Simmer, C., Belyaev, K., Kapala, A., & Gulev, S. (2009). Improving estimates of heavy and extreme precipitation using daily records from European rain gauges. Journal of Hydrometeorology, 10(3), 701-716. https://doi.org/10.1175/2008JHM1055.1.

65. Zolina, O., Simmer, C., Gulev, S. K., & Kollet, S. (2010). Changing structure of European precipitation: longer wet periods leading to more abundant rainfalls. *Geophysical Research Letters*, *37*(6). https://doi.org/10.1029/2010GL042468.

66. Zolina, O., Simmer, C., Kapala, A., & Gulev, S. (2005). On the robustness of the estimates of centennial-scale variability in heavy precipitation from station data over Europe. Geophysical Research Letters, 32(14). https://doi.org/10.1029/2005GL023231.

67. Zolina, O., Simmer, C., Kapala, A., Bachner, S., Gulev, S., & Maechel, H. (2008). Seasonally dependent changes of precipitation extremes over Germany since 1950 from a very dense observational network. Journal of Geophysical Research: Atmospheres, 113(D6). https://doi.org/10.1029/2007JD008393.

Table 1. Cross-validation results for kriging, Inverse Distance Weighting (IDW), Heylock *et al.* (2008) method, and Thin Plate Spline (TPS). These results are median values computed from comparing daily observations with estimates employing the mean absolute error as accuracy index.

Year	**Method**			
	Kriging	IDW	Haylock *et al.*	TPS
2000	0.59	0.5	0.5	0.64
2001	0.63	0.61	0.56	0.79
2002	0.35	0.29	0.26	0.41
2003	0.76	0.67	0.75	0.88
2004	0.44	0.41	0.53	0.6
2005	0.54	0.43	0.43	0.62
2006	0.43	0.42	0.44	0.53
2007	0.29	0.25	0.24	0.39
2008	0.28	0.22	0.21	0.33
2009	0.44	0.4	0.41	0.47
2010	0.32	0.26	0.24	0.33
2011	0.78	0.76	0.7	0.89
2012	0.28	0.25	0.28	0.36
2013	0.35	0.33	0.24	0.39
2014	0.33	0.28	0.25	0.43
Mean	0.454	0.405	0.403	0.537

Table 2. The precipitation extreme indices as proposed by ETCCDI (Zhang et al. 2011).

Number	Index	Indicator name	Definition	Unit
1	R10mm	Number of heavy precipitation days	Count of days when PR>=10 mm	day
2	R20mm	Number of very heavy precipitation days	Count of days when PR >=20 mm	day
3	CDD	Consecutive dry days	Maximum number of consecutive days with PR<1 mm	day
4	CWD	Consecutive wet days	Maximum number of consecutive days with PR>=1 mm	day
5	SDII	Simple daily intensity index	Total precipitation divided by number of wet days in the year	mm day^{-1}
6	R95pTOT	vey wet days	Total PR when RR>95th percentile	mm
7	R99pTOT	Extremely wet days	Total PR when RR>99th percentile	mm
8	R95pDay	vey wet days	Count of days when RR>95th percentile	day
9	R99pDay	Extremely wet days	Count of days when RR>99th percentile	day
10	RX1day	Max 1-day precipitation amount	Maximum 1-day precipitation	mm
11	RX5day	Max 5-day precipitation amount	Maximum consecutive 5-day precipitation	mm

Table 3. Percentage of grid cells with insignificant (Ins) different mean (MW and t-student tests) and variance (Levene and F tests) at significance level of 5% and spatiotemporal averaged correlation coefficient for NWD, TOT, and INT at different time scales, 2000-2014.

		Winter	Spring	Autumn
MW Ins. %	NWD	36.1	82.8	93.5
	TOT	89.4	93.5	97.6
	INT	53.3	91.7	89.9
t-Studend Ins. %	NWD	32.0	82.3	32.0
	TOT	89.9	91.7	89.9
	INT	53.3	90.5	53.3
Levene Ins. %	NWD	87.0	85.2	57.4
	TOT	99.4	97.0	87.0
	INT	72.2	85.2	79.3
F test Ins. %	NWD	82.8	88.8	82.8
	TOT	97.0	97.6	97.0
	INT	50.3	77.5	50.3
Correlation	NWD	0.49	0.80	0.61
	TOT	0.91	0.90	0.72
	INT	0.67	0.60	0.54

Table 4. Percentage of grid cells with insignificant (Ins) different mean (MW and t-student tests) and variance (Levene and F tests) and spatiotemporal averaged correlation coefficient for R10mm and Rx1Day at different time scales at siginificance level of 5%, 2000-2014.

		Winter	Spring	Autumn
MW Ins %	R10mm	89.35	89.94	100
	Rx1Day	88.76	95.86	100
t-Studend Ins %	R10mm	88.17	89.35	100
	Rx1Day	87.57	95.27	98.22
Levene Ins %	R10mm	92.31	94.08	82.25
	Rx1Day	84.62	95.86	93.49
F test Ins %	R10mm	86.39	95.27	86.98
	Rx1Day	71.6	94.08	94.67
r	R10mm	0.72	0.75	0.63
	Rx1Day	0.62	0.69	0.6
BR	R10mm	0.82	1.02	1.02
	Rx1Day	1.16	1.08	1.3

Table S1. List of Meteorological rain gauge stations along with their geographic characteristics and statistics for the respective annual precipitation in period of 2000 to 2014.

No	Station	Lon (°)	Lat (°)	Alt (m)	Mean Annual (mm)	Min	Max	Standard Deviation
1	Goshnegan-Maharloo	52.88	29.5	1440	452	67.8	228.6	101.4
2	Mooroozeh	51.9	30.17	1946	1048.5	271	575.6	199.3
3	Barghan	52.02	30.21	2109	1175.5	286.5	625	228.3
4	Batoon	51.32	30.24	751	948.5	211.8	533.4	203.2
5	Mal-Ghayedi	52.02	30.04	1639	951	226	481.9	179.7
6	Babamonir	51.21	30.08	1033	826	137	433.2	174
7	Booshigan-Kazeroon	51.51	29.73	735	706	116.5	403	146.3
8	Kazeroon	51.66	29.61	841	857.5	130.2	416.3	177.3
9	Dasht-Arzhan	51.99	29.66	2029	1436.5	353	729	276
10	Nargesi	52.05	29.26	933	607	88	288.7	120.5
11	Jareh	51.98	29.25	868	702.5	103	314.8	141.2
12	Farashband	52.08	28.84	805	539	53.5	225.1	110
13	Chiti-Boorki	51.31	29.6	490	703	87	317.2	144.7
14	Ghaemieh	51.6	29.84	915	1014.5	162.5	522.7	203.1
15	Khormayek	52.05	28.77	781	523	49	216.5	109.1
16	Sarmashhad	51.71	29.29	822	660.5	81.5	280.5	134.1
17	Band-Bahman	52.57	29.21	1597	872.5	128.5	401.8	181.9
18	Aliabad-Khafr	53.03	29.02	1368	590	63.5	258.9	132.2
19	Karian	53.54	28.15	843	382.5	68.5	194	91.2
20	Fasa	53.65	28.93	1370	560.9	57.4	245.4	124.4
21	Soroor	53.75	28.47	1347	758	93.5	324.8	160.8
22	Tang-Karzin-Dohbe	53.13	28.45	712	502	94.5	245	105.9
23	Mobarakabad	53.33	28.36	715	493	55	221.9	114.2
24	Hanifghan	52.56	29.09	1598	851	133	391.4	169.7
25	Tongab-Firoozabad	52.54	28.91	1376	971.5	113	405	192.3
26	Roniz-Olya	53.78	29.2	1597	564	72.5	223	124.8
27	Jahrom	53.56	28.5	1047	497	69.5	245.7	111.7
28	Khanzenyan	52.15	29.67	1966	738	210.5	440.8	143.8
29	eej	54.24	29.03	1495	339	43	216.3	90.6
30	Baba-arab	53.8	28.59	1160	432.5	65.8	190.5	100.2
31	Khoorab	52.32	28.6	606	468	38.5	222.3	109.9
32	Hakkan	53.42	28.62	966	592.5	88	271.3	127.8
33	Dezhgah	52.39	28.2	223	283	35.9	143.6	68.8
34	Khorgheh	52.38	28.91	1590	1163.5	142	501.9	226.4
35	Dahvieh	52.74	28.68	1372	721	92	346.4	146.1
36	Sheshdeh-Gharebolagh	53.96	28.96	1411	537.5	64.5	252	110.5
37	Hengam	52.6	28.37	560	445	61.5	217.4	97.6
38	Ooz	54.01	27.77	969	296.5	61.5	186.4	73.7
39	Jookan	52.58	29.04	1528	767.5	110	344.9	153.5

40	Dehkooyeh	54.42	27.86	1010	238	59.5	156	63.4
41	Hasanabad-Marmeh	53.91	28.07	873	276	37	159.6	83.1
42	Garebayegan	53.92	28.61	1154	401	64	198.2	101.1
43	Myanjangal	53.42	29.16	1713	897	104	352	189.1
44	Dehrood-Firoozabad	52.57	28.62	903	462.5	53	221.6	108
45	Gavazoon	54.45	28.82	1239	523.2	94.4	265.3	108.4
46	Dehkheir-Jannatshahr	54.68	28.66	1173	370	85.5	221.8	95.8
47	Darbeghaleh	54.38	28.95	1422	519	96.3	257.9	111.4
48	Hajiabad-Zarindasht	54.43	28.35	1067	298	57	186.5	80.1
49	Forg	55.21	28.28	928	253.5	47	147.5	58.7
50	Edareh-Lar	54.31	27.65	841	248.1	59	154	63.9
51	Lamerd	53.16	27.34	450	351.8	76.5	183.6	88.2
52	Layezangan	54.98	28.67	1967	598	151	423.5	141.3
53	Menj	53.9	30.36	1865	237.5	50	126.1	59.2
54	Mazayjan-Bavanat	53.81	30.3	2128	401.5	61.5	201	91
55	Meshkan	54.33	29.48	2215	523.5	86.5	268.2	114.1
56	Sadegh-Abad	52.32	31.16	2361	461	38.5	206.2	97.2
57	Soorian	53.63	30.47	2136	424.5	75	184.1	100.9
58	Mehrabad-Ramjerd	52.7	29.97	1606	732.3	138.3	329.7	146.8
59	Jamalbeig	51.95	30.61	2010	784	203.5	479.7	165.9
60	Chamriz	52.1	30.47	1810	833	157	415.7	168.3
61	Bidkol	52.63	30.17	1626	744	145.5	361	152.6
62	Kaftar	52.73	30.53	2342	971	191.5	471.9	207
63	Jahanabad-Bakhtegan	53.86	29.71	1577	481.4	82	216.6	98.2
64	Arsanjan	53.32	29.92	1648	603.5	75	268.8	144.6
65	Dashtbal	52.98	30	1673	710	117.8	311.6	146.5
66	Ghalat-Shiraz	52.35	29.84	1881	1090	222	530.2	210.9
67	Polekhan	52.77	29.85	1493	664.5	92.5	276.3	139.9
68	Shiraz	52.53	29.63	1522	730.5	129.9	333.2	147.4
69	Dobaneh	52.78	29.42	1489	855.5	137.5	359	175.5
70	Khosroshirin	52.01	30.9	2342	702.5	127.5	382.3	145.2
71	Garde-Estahban	53.88	29.16	1698	841.5	96.5	341.6	191.6
72	Doshmanziari	52.37	30.08	1663	781	144	385.5	159.4
73	Choobkhale	51.89	30.55	2056	1318.5	377.5	845.8	270
74	Abade-Tashk	53.73	29.81	1604	532	77	234.3	121.5
75	Ahmadabad-Chahardangeh	52.69	30.39	2275	744.5	134.5	332.1	160.5
76	Sahlabad	53.9	29.26	1518	403	52	181.2	84.4
77	Doroodzan	52.44	30.21	1662	786	193	423.9	160.4
78	Madarsoleiman	53.18	30.19	1868	610.5	120	305.3	133.3
79	Estahban	54.05	29.12	1745	704	82.9	299.7	157.3
80	Hosseinabad-Sarab	52.36	29.97	1695	747.5	168	395.6	143.5
81	Neiriz	54.35	29.19	1657	378	57	164.6	78.1
82	Sarvestan	53.22	29.28	1570	432	60.5	205.8	90.7
83	Emamzadeh-Esmaeel	52.59	30.32	1842	859.5	193	459.7	172.4

84	Dashtak	52.47	30.29	2031	784	219	447.3	154.6
85	Horgan	54.47	29.11	1898	649.5	84.5	279.3	145.2
86	Kholar	52.24	29.97	2056	1112	287	574.7	228.6
87	Sedeh	52.16	30.72	2198	829.5	136.7	446	184
88	Komahr	51.88	30.45	2354	1789	431	1007.3	367.6
89	Poltalkh	53.43	29.46	1592	359.5	55	152.1	77.5
90	Fenjan	53.49	30.39	2376	657	135	327.7	137

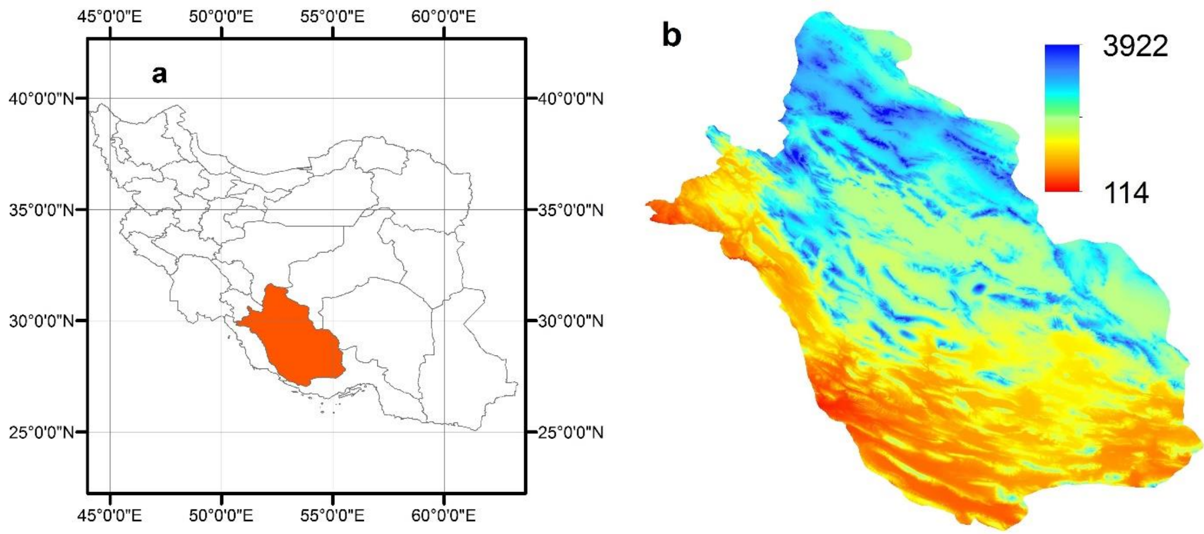

Figure 1. (a) Geographic location of Fars province in I.R. of Iran; (b) Elevation map of Fars province (m).

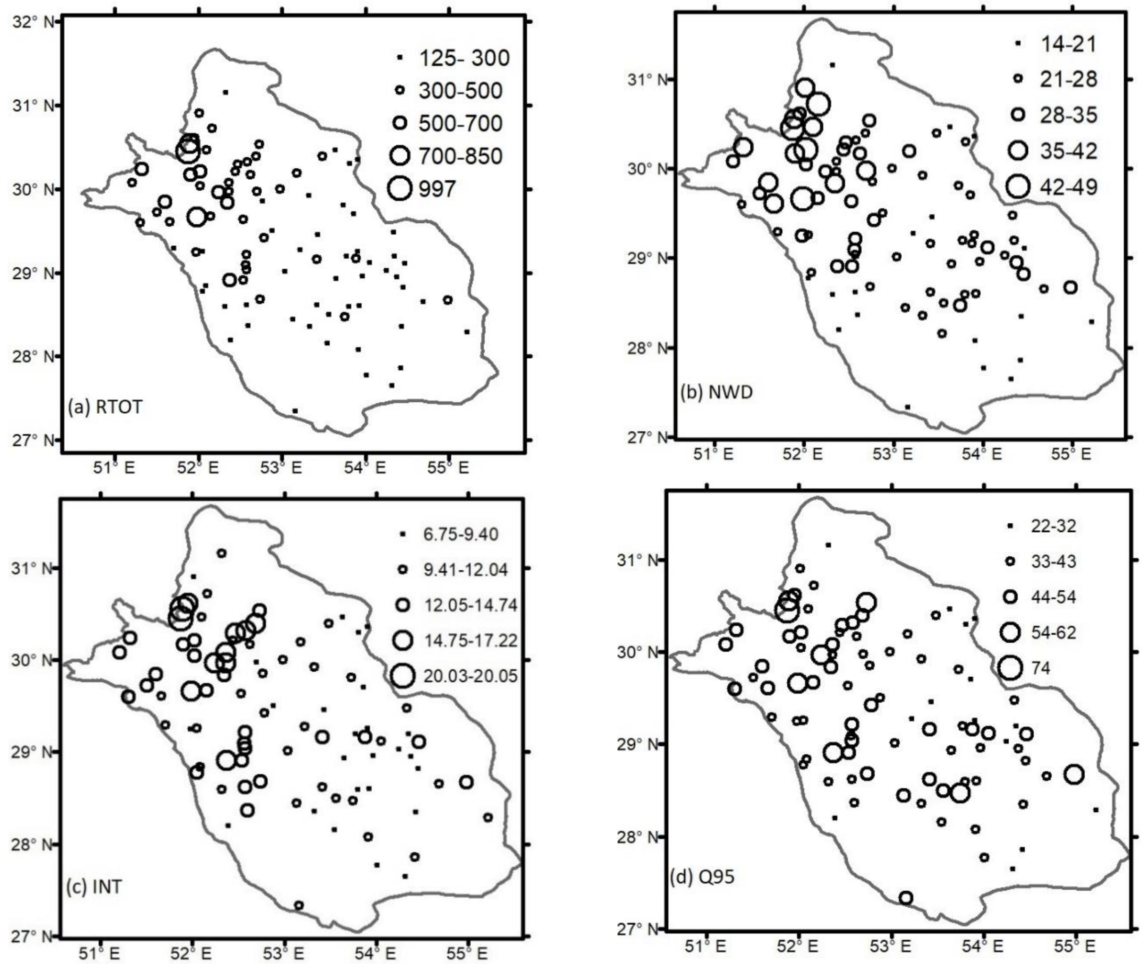

Figure 2. (a) Average of annual precipitation (RTOT, mm), (b) mean number of wet days in a year (NWET, day) (c) average of annual precipitation over all wet days (INT, mm day^{-1}), (d) and 95th percentile from the empirical (wet day) distribution functions (Q95, mm), for the rain gauges of Far province, 2000-2014.

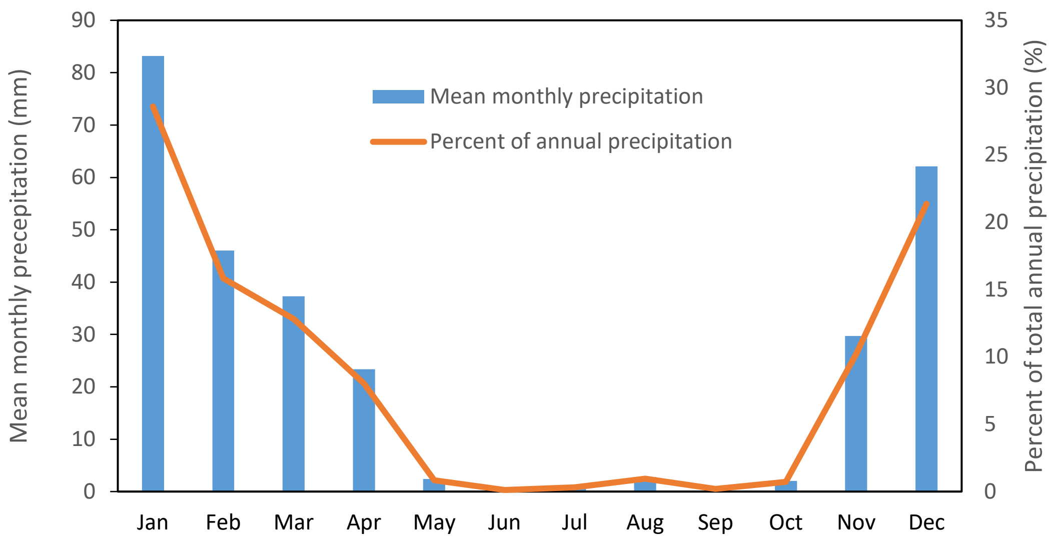

Figure 3. The climatological mean of monthly precipitation (mm) and the percentage of annual precipitation across the Fars province, 2000 – 2014.

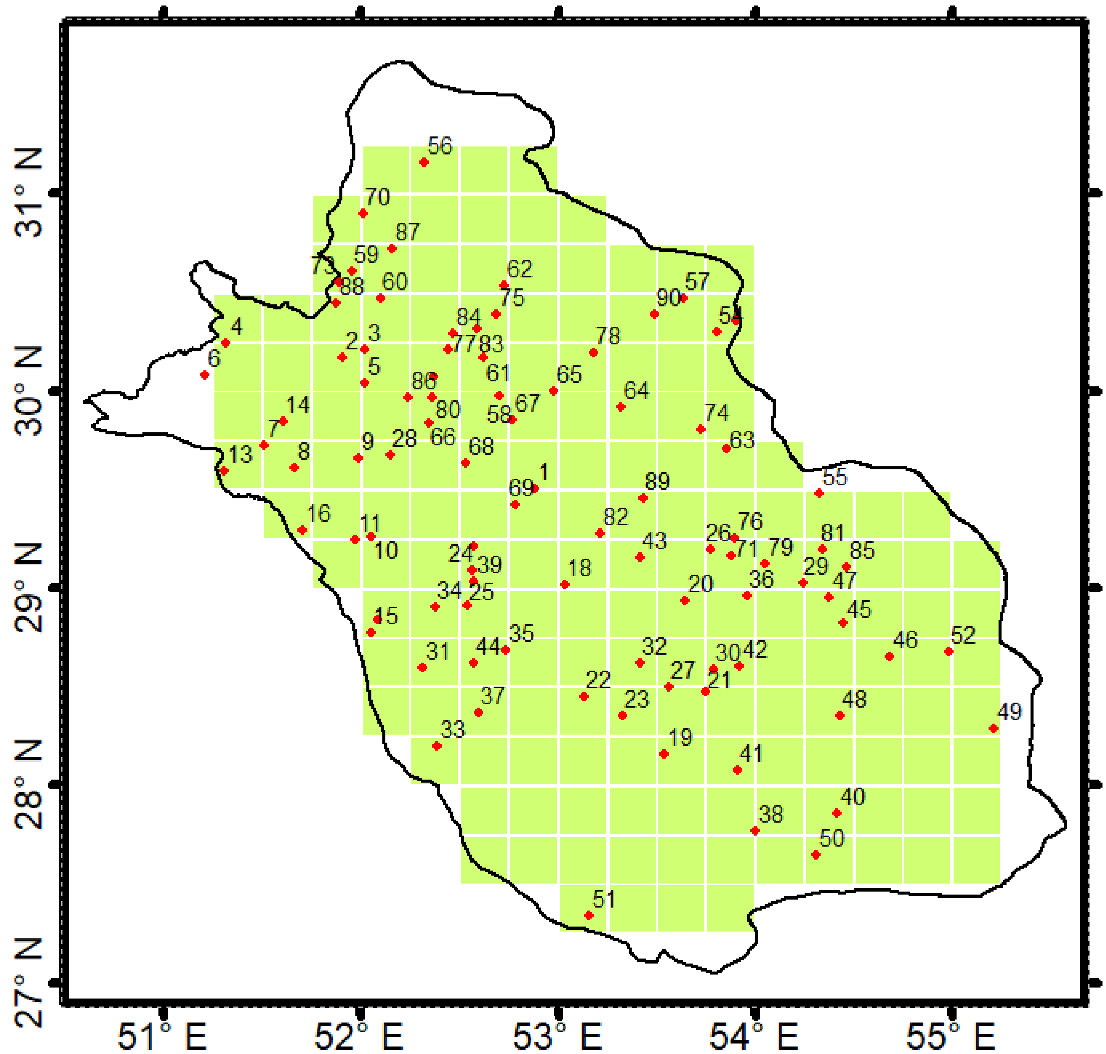

Figure 4. Geographic location of rain gauges and 3B42 grid cells across Fars province.

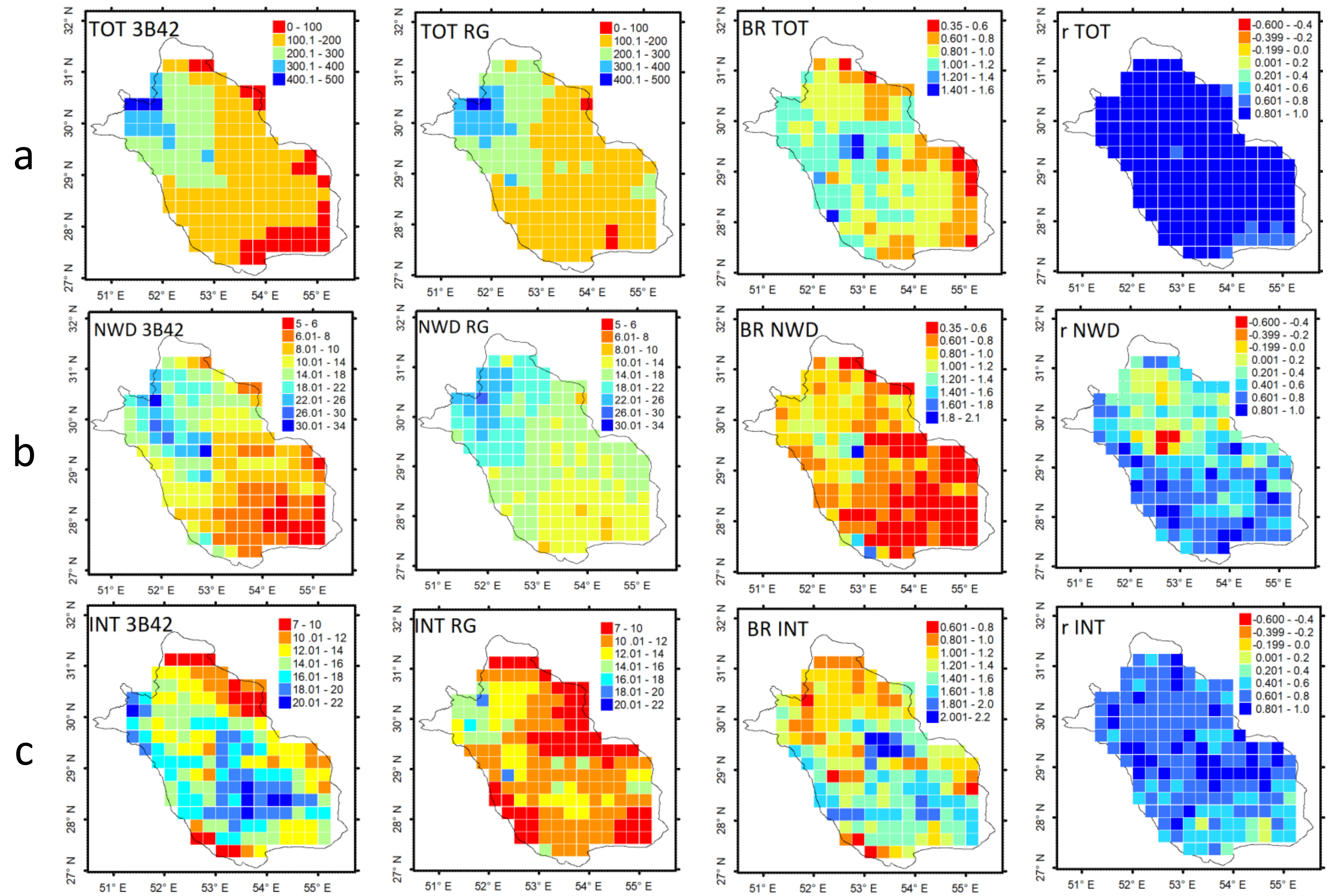

Figure 5. (a) Climatological mean total precipitation (mm), (b) mean number of wet days (day/season), (c) mean wet-day intensity (mm/day) based on winter season (DJF) of the entire time period (2000-2014) for 3B42 estimates (first column), RG results (second column), bias ratio (3B42/RG, third column), and Pearson correlation coefficient (forth column).

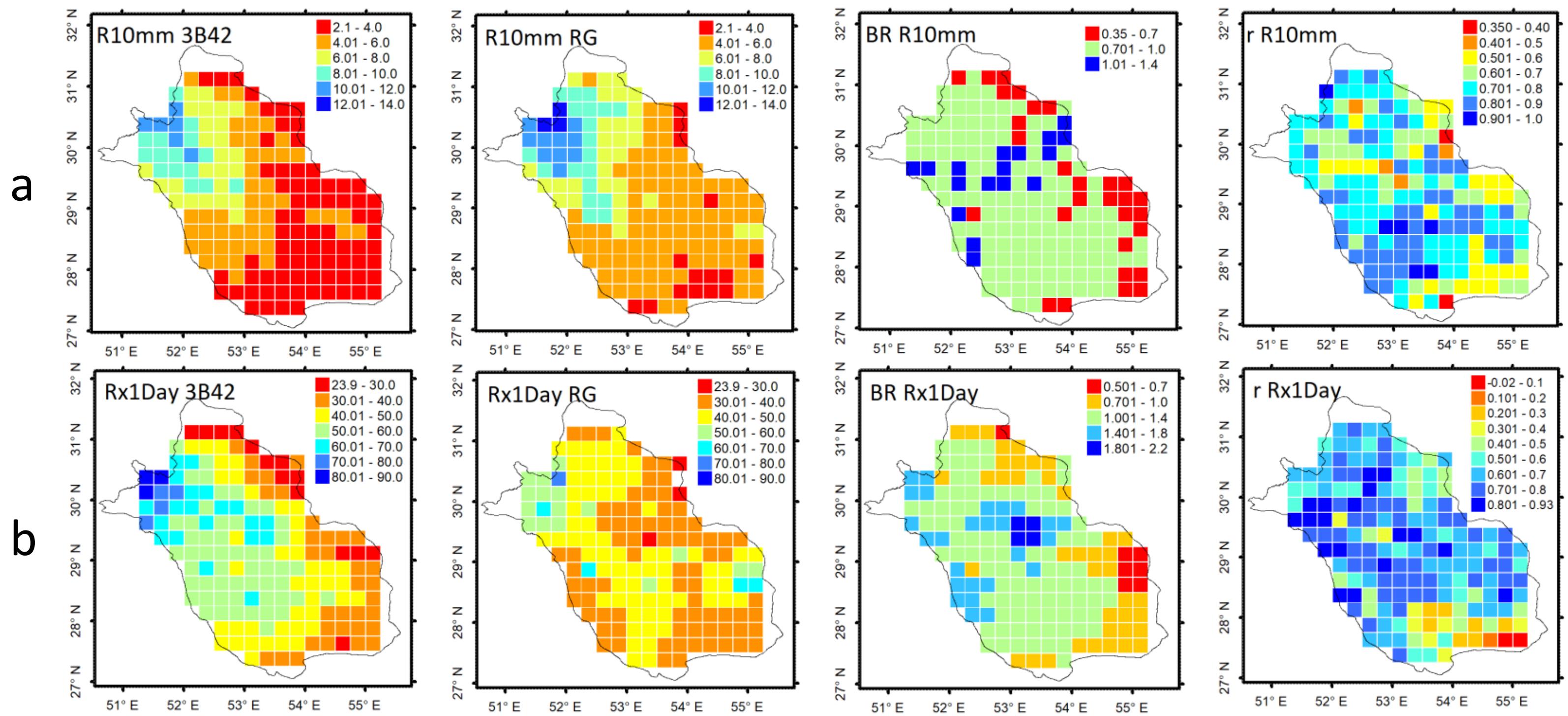

Figure 6. (a) Mean R10mm and (b) mean Rx1Day based on winter season (DJF) of the entire time period (2000-2014) for 3B42 estimates (first column), RG results (second column), bias ratio (3B42/RG, third column), and Pearson correlation coefficient (forth column).

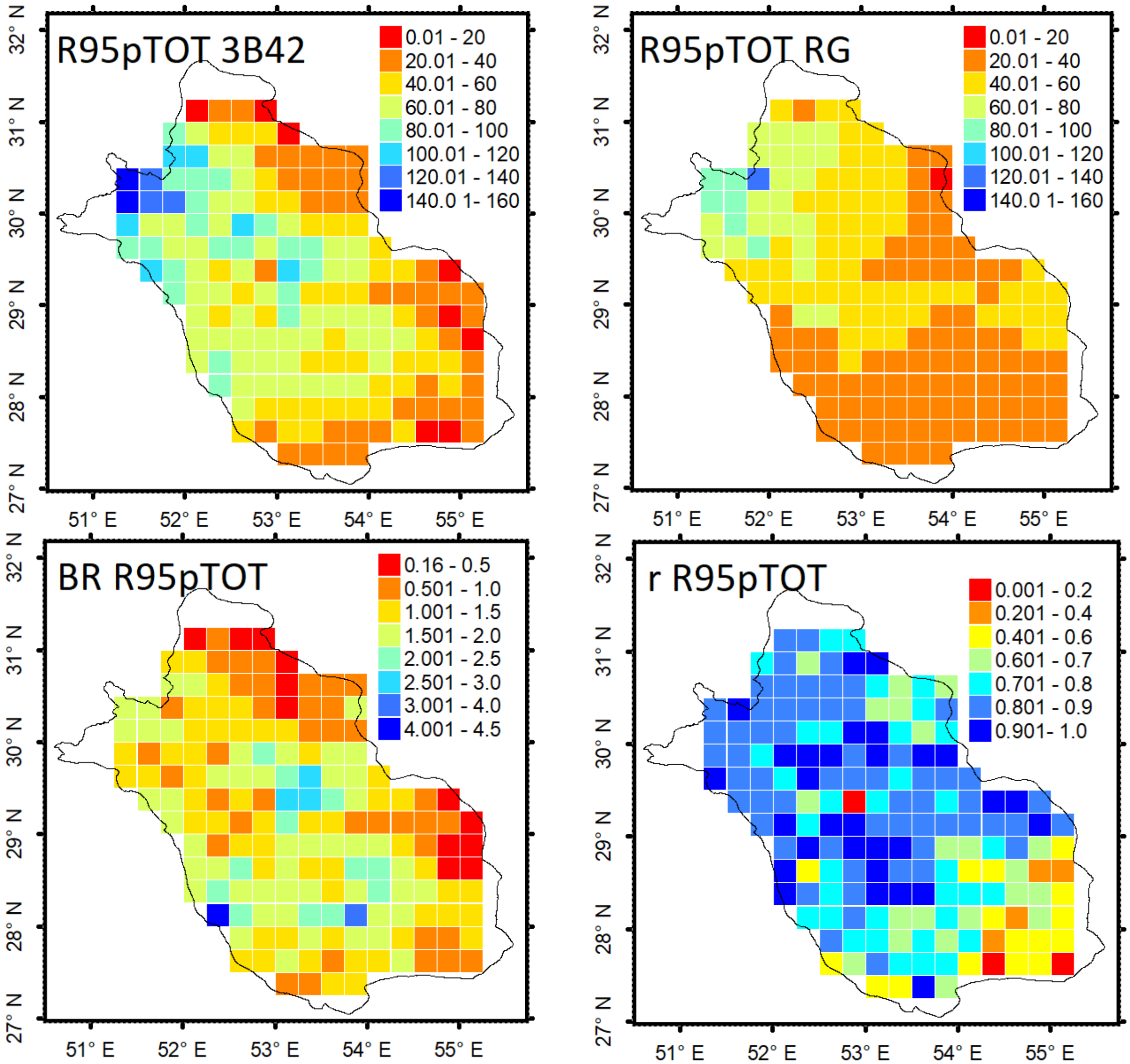

Figure 7. Spatial distribution of R95pTOT obtained from 3B42 and RG with bias ratio (BR) and Pearson correlation coefficient (r) for winter (DJF) for the period 2000-2014.

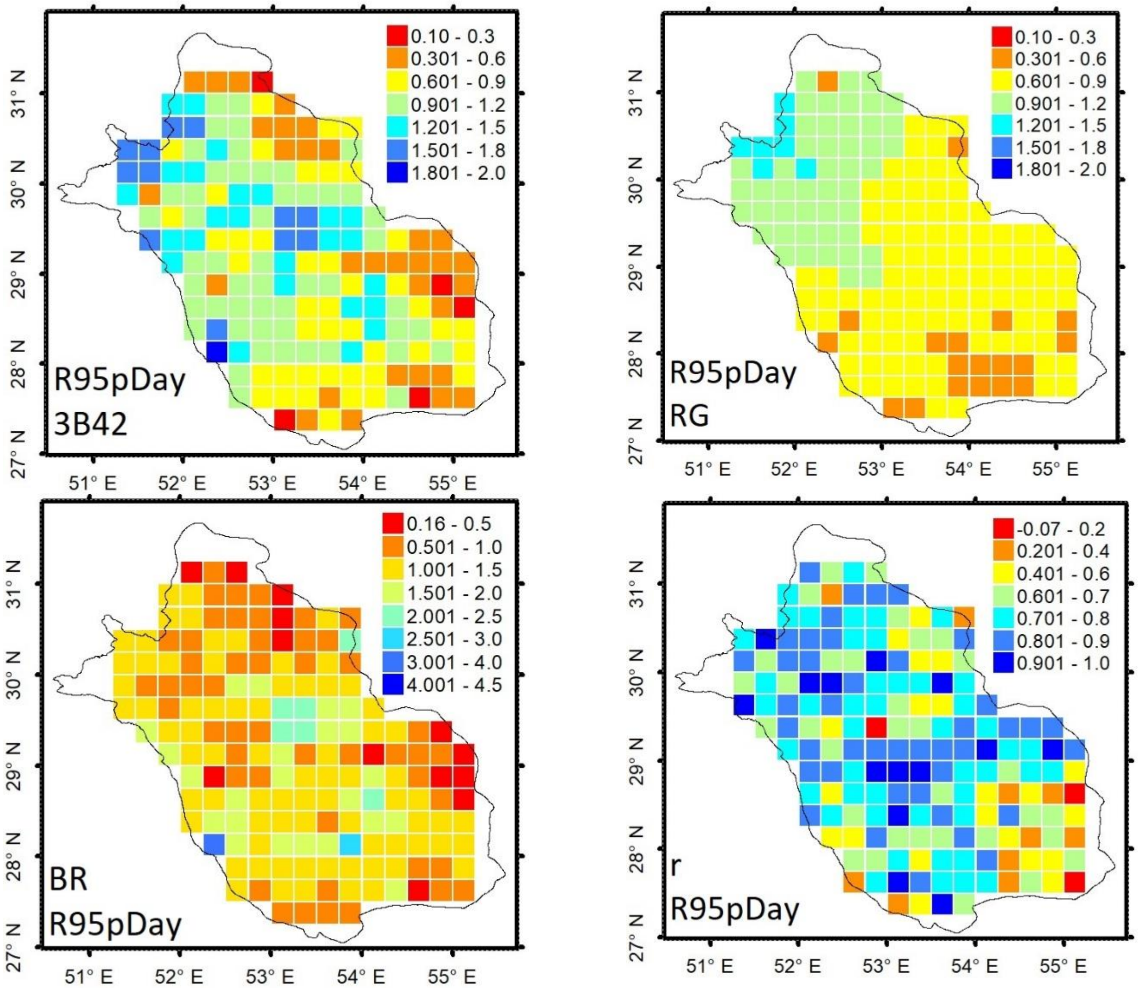

Figure 8. Spatial distribution of R95pDay obtained from 3B42 and RG with bias ratio (BR) and Pearson correlation coefficient (r) for winter (DJF) for the period 2000-2014.

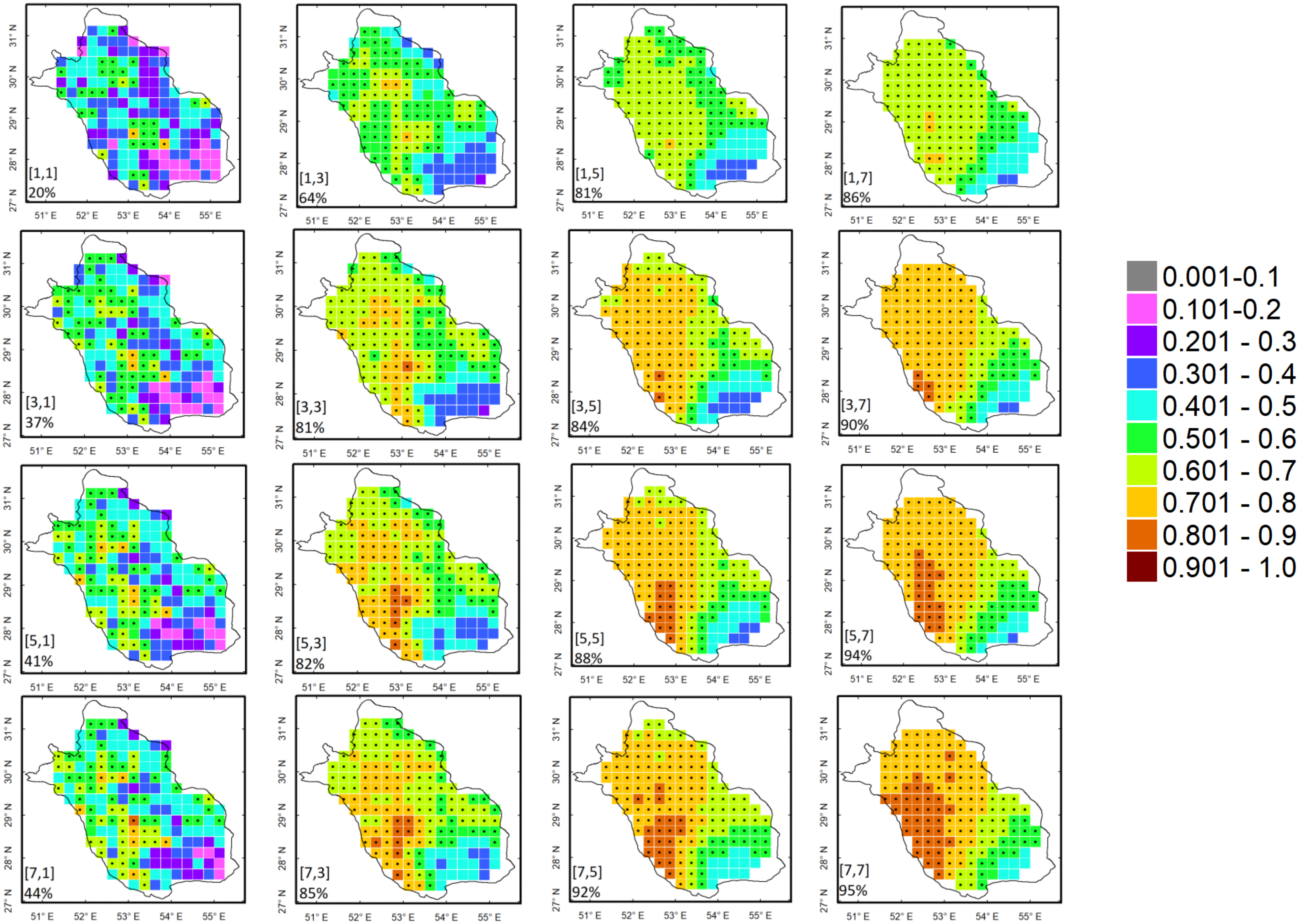

Figure 9. FSS based on the 95th percentile threshold for the winter season (DJF) as a function of increasing temporal (1,3,5, and 7 days; first numbers in brackets) and spatial (1, 3, 5, and 7 pixels; second numbers in brackets) size of the neighborhood. The numbers beside % sign indicate the relative number of grid boxes (%) with FSS values exeedind the local FSS_{useful} and the points in the maps indicate the location of these pixels.

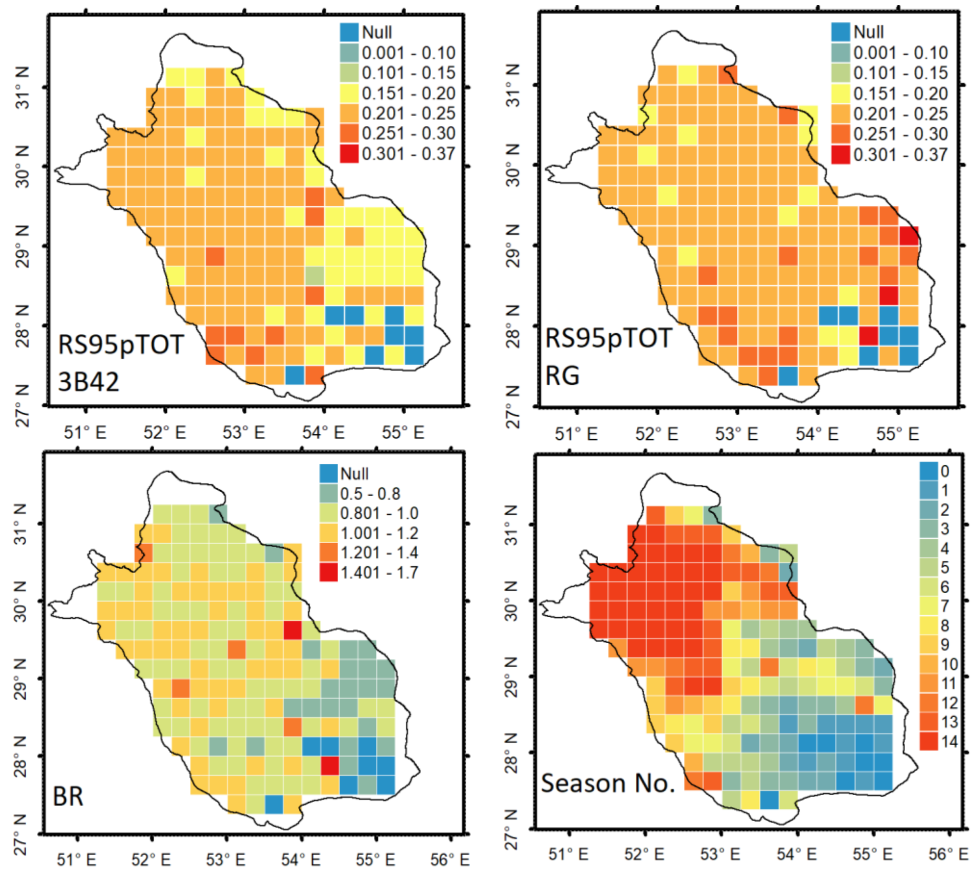

Figure 10. Climatological (2000-2014) mean of RS95pTOT for winter (DJF) with coresponding values of mean bias ratio (BR) and number of cosiderderd winter (DJF) seasons.

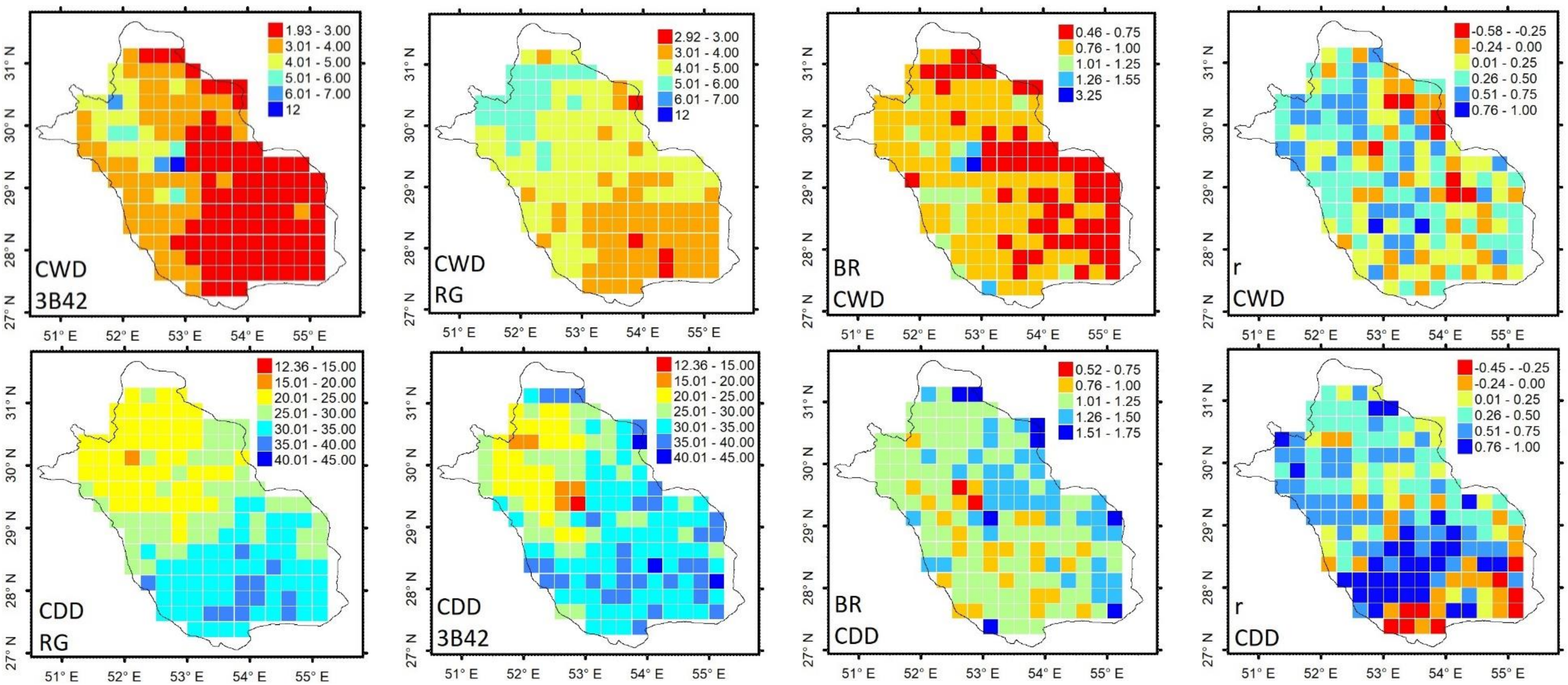

Figure 11. Spatial variation of mean CDD and CWD, with bias ratio (BR) , and Pearson correlation coefficient (r) for each, the values are averages for the wet season (October-March) 2000-2014.

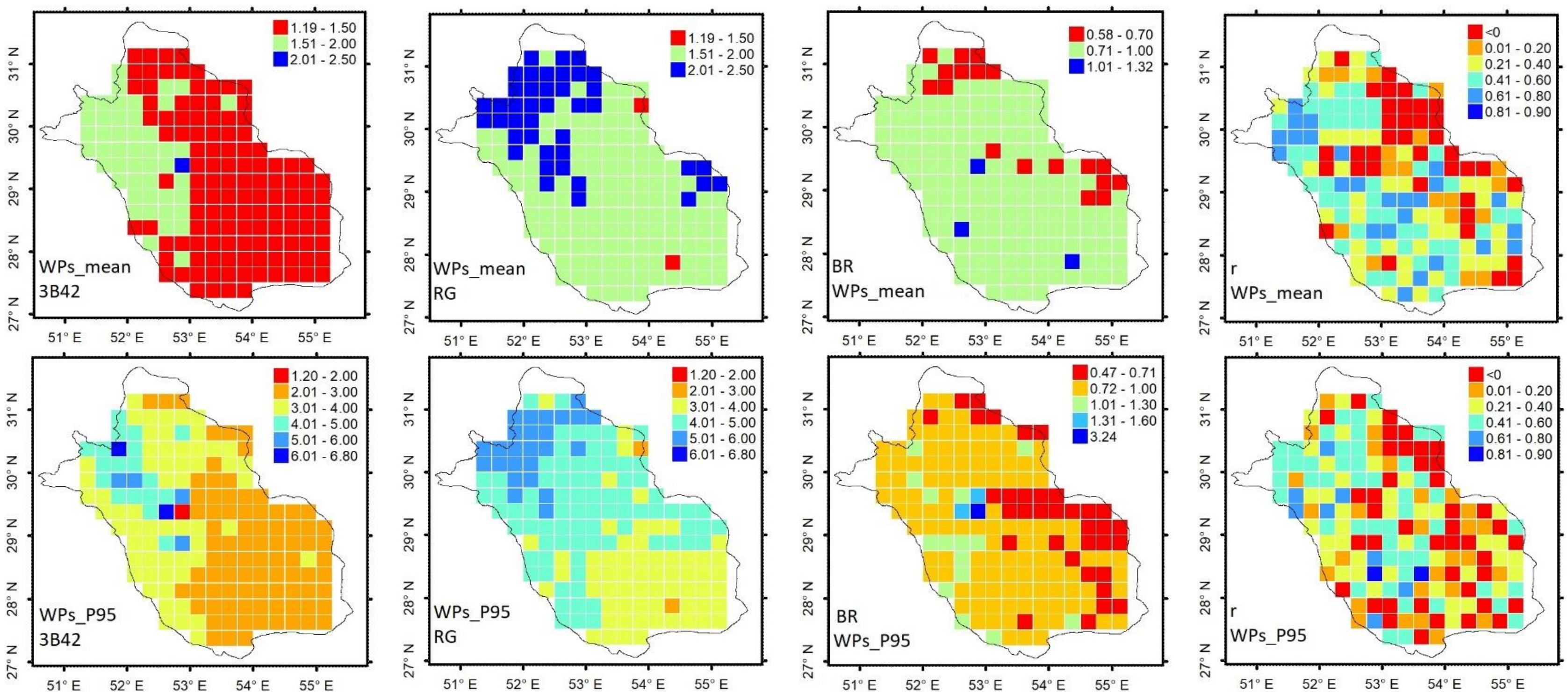

Figure 12. Distribution of the mean duration (WPs_mean), 95 percentile (WPs_P95) of wet spells obtained from TGD based on 3B42 and RG datasets and bias ratio (BR) Pearson correlation coefficient (r), all maps are for wet season (October-March), 2000-2014.

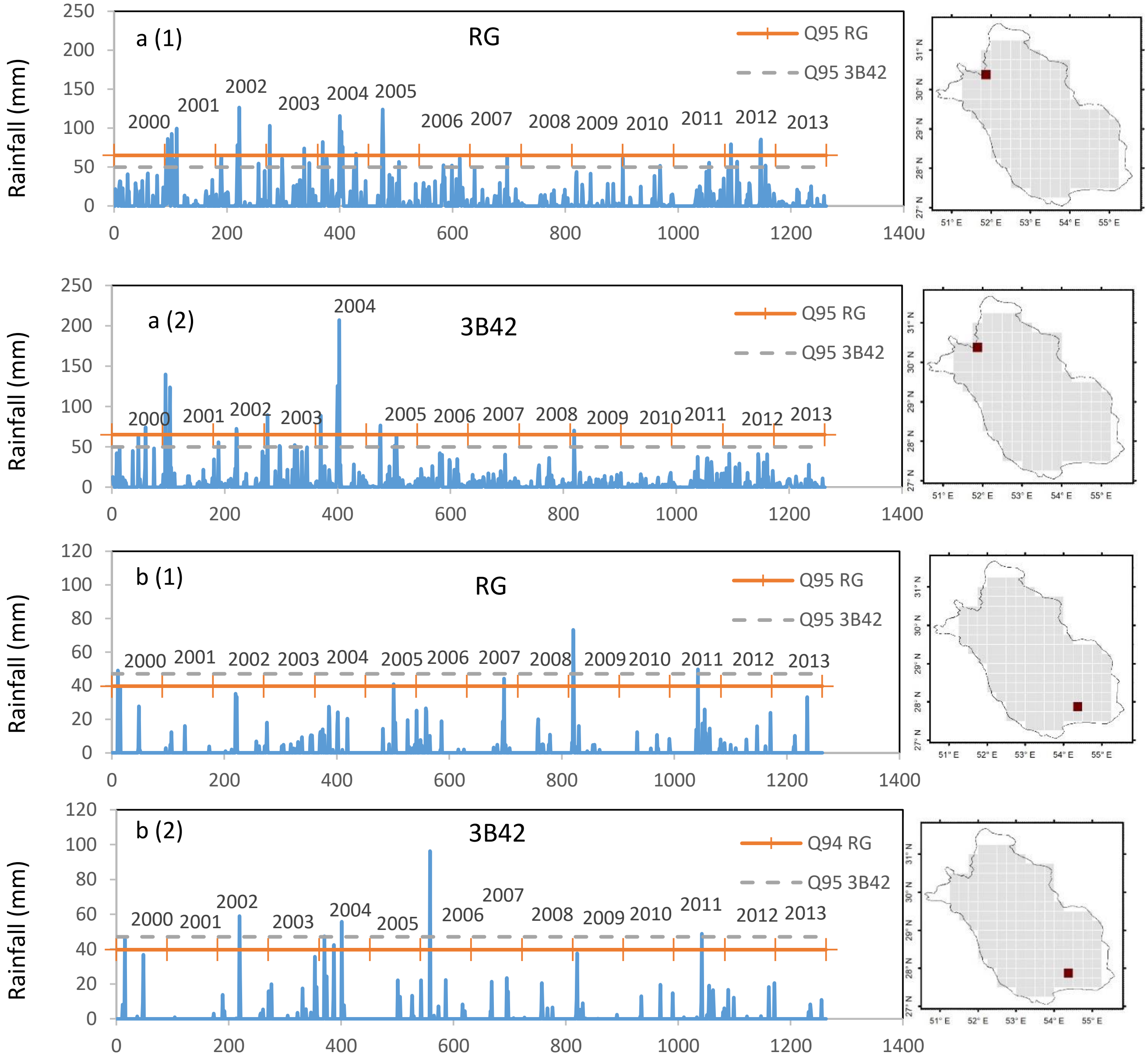

Figure 13. Time series of daily precipitation at two locations (a) 30.375°N,51.875°E and (b) 27.875°N,54.375°E for 14 winter seasons as depicted by (1) RG and (2) 3B42.

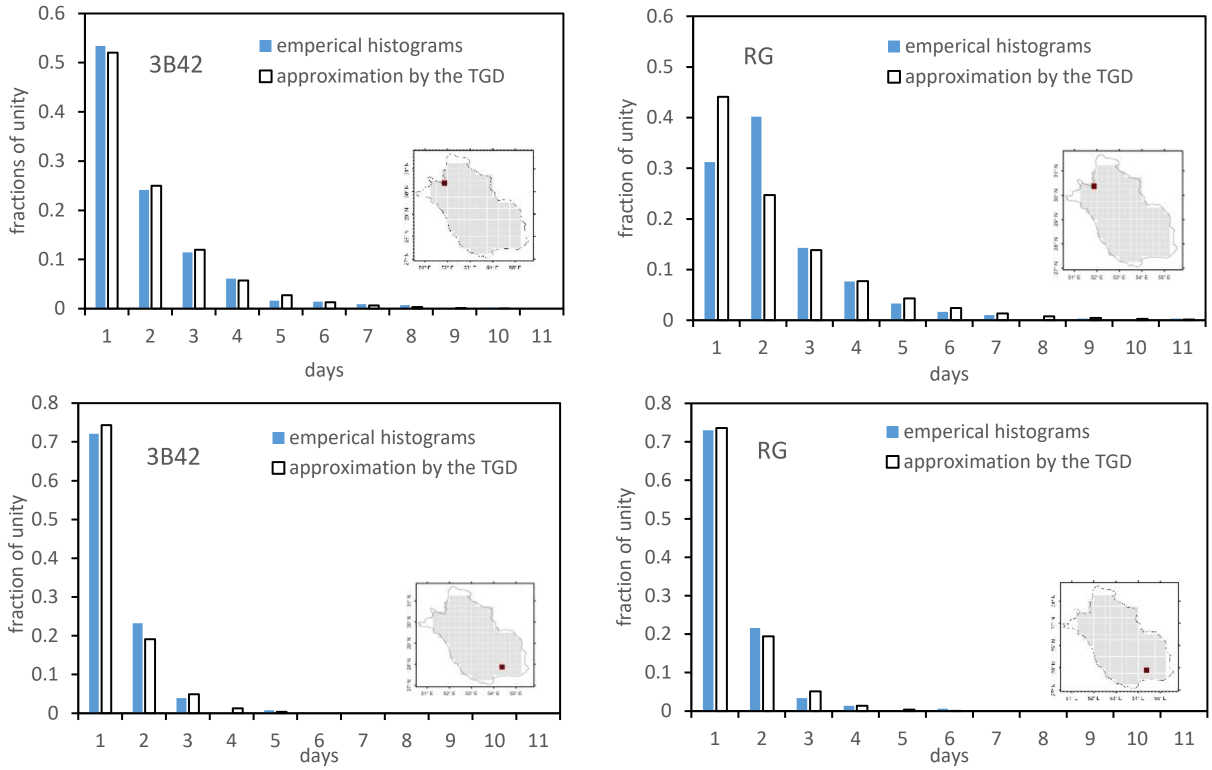

Figure 14. Examples of empirical histograms of WPs durations for the two selected grid cells (dark pixels in the maps) for wet season (October-March) during 2000-2014, as well as their approximation by the TGD.